AUTO-CONTROL HYPERTHERMIA APPLICATIONS OF LAFESIH NANOPARTICLES WITH FIRST-ORDER PHASE TRANSITION

BİRİNCİ DERECEDEN FAZ GEÇİŞİNE SAHİP LAFESİH NANOPARÇACIKLARININ OTO-KONTROL HİPERTERMİ UYGULAMALARI

MERVENUR KELEŞ

ASSOC. PROF. TELEM ŞİMŞEK

Supervisor

Submitted to

Graduate School of Science and Engineering of Hacettepe University

as a Partial Fulfillment to the Requirements

for the Award of the Degree of

Master of Science

in Nanotechnology and Nanomedicine.

2024

ABSTRACT

AUTO-CONTROL HYPERTHERMIA APPLICATIONS OF LAFESIH NANOPARTICLES WITH FIRST-ORDER PHASE TRANSITION

Mervenur KELEŞ

Master of Science, Nanotechnology and Nanomedicine Division

Supervisor: Assoc. Prof. Telem ŞİMŞEK

January 2024, 65 pages

Magnetic hyperthermia applications demand precise temperature control within the targeted region to safeguard the well-being of surrounding healthy tissues during cancer treatments.To achieve this objective, a temperature control mechanism can be implemented based on the heating properties of magnetic nanoparticles, which is called auto-control magnetic hyperthermia. This can be accomplished by utilizing magnetic materials that undergo a first-order phase transition around the Curie temperature. LaFeSi compounds, well-known for their magnetocaloric applications, have the potential to be employed as a material for auto-control magnetic hyperthermia therapy applications. However, Curie point of LaFeSi compound is significantly lower than the necessary temperature required to eradicate cancerous cells. In this thesis, we studied on a method to elevate the Curie temperature of LaFeSi compounds to points adequate for inducing protein denaturation in cancer cells through heating, achieved by hydrogenation of the compound. For this purpose, $LaFe_{11.57}Si_{1.43}$ ingots are initially fabricated using the arc-

melting technique. Subsequently, the compounds exposed to high-temperature heating for several days to ensure homogenization. Samples are then hydrogenated under 5 bar H_2 atmosphere using a Sievert-type apparatus. Following this, the samples are annealed under vacuum conditions for varying durations to fine-tune the Curie temperature of the compounds. Samples are also mechanically milled to obtain nanoparticles.

The Curie temperature is succesfully tuned from 200 K to 341 K by changing the H amount in $LaFe_{11.57}Si_{1.43}H_y$ compounds. The $LaFe_{11.57}Si_{1.43}H_{1.41}$ samples with cubic $NaZn_{13}$-type structure, demonstrated efficient heating capabilities. Remarkably, the samples retain 1st-order magnetic phase transition characteristics and cease heating around 50 °C when subjected to an alternating magnetic field. The specific absorbtion rate is therapeutically significant, 10.9 W/g at an applied field of 26 kA/m and a frequency of 300 kHz. Given these exceptional properties, LaFeSiH compounds emerge as promising candidates for deployment as therapeutic materials in cancer treatment.

Keywords: auto-control hyperthermia, 1st-order Curie phase transition, LaFeSiH compound, magnetic nanoparticles.

ÖZET

BİRİNCİ DERECEDEN FAZ GEÇİŞİNE SAHİP LAFESIH NANOPARÇACIKLARININ OTO-KONTROL HİPERTERMİ UYGULAMALARI

Mervenur KELEŞ

Yüksek Lisans, Nanoteknoloji ve Nanotıp ABD

Tez Danışmanı: Doç. Dr. Telem ŞİMŞEK

Ocak 2024, 65 sayfa

Manyetik hipertermi ile kanser tedavisinde, tümör çevresindeki sağlıklı dokuların güvenliği için hedeflenen bölgedeki sıcaklığın kontrol altına alınmasına ihtiyaç vardır. Bunu sağlamak için, manyetik nanoparçacıkların ısıtma mekanizmalarına dayalı bir sıcaklık kontrolü yapılabilir. Otokontrol manyetik hipertemi olarak adlandırılan bu olgu, Curie sıcaklığı 1. dereceden faz gösteren manyetik malzemeler kullanılarak gerçekleştirilebilir. Manyetokalorik uygulamalarıyla bilinen 1. Dereceden geçişe sahip LaFeSi bileşikleri, otokontrol manyetik hipertermi uygulamaları için yüksek potansiyele sahiptir. Ancak LaFeSi bileşiğinin Curie sıcaklığı, kanserli hücreleri yok etmek için gereken sıcaklıktan çok daha düşüktür. Bu tezde, $LaFe_{11.57}Si_{1.43}$ bileşiğinin Curie sıcaklığını kanser hücrelerinde protein denatürasyonunu gerçekleştirecek sıcaklıklara yükseltmek için, bileşiğe H katkılaması üzerine çalışıldı. Bu amaçla, yığın LaFeSi bileşiği ark eritme tekniği kullanılarak üretildi. Daha sonra homojenizasyon için bileşiklere yüksek sıcaklıkta ısıl işleme uygulandı. Daha sonra örneklere Sievert tipi cihaz kullanılarak, 5 bar H_2 atmosferinde hidrojen katkılandı. Ardından örnekler, Curie

sıcaklıklarının değiştirilmesi amacıyla vakum koşulları altında değişen sürelerde tavlandı. Ardından örnekler mekanik öğütme ile nanoboyuta küçültüldü.

Sonuçlar hidrojen katıkılaması ile örneklerin Curie sıcaklığının 200 K ila 341 K arasında başarılı bir şekilde değiştirilebildiğini gösterdi. İyi ısıtma verimi sergileyen kübik $NaZn_{13}$ tipi $LaFe_{11.57}Si_{1.43}H_{1.41}$ örneğin, alternatif manyetik alan altında 50 °C civarında 1. dereceden faz geçiş özelliğini koruyarak ısıtmayı kendiliğinden durduğunu gözlendi. 26 kA/m şiddetli ve 300 kHz frekansında uygulanan manyetik alan varlığında, örneğin öz soğurma oranı 10,90 W/g olarak hesaplandı. Bu özellikleriyle üretilen LaFeSiH bileşiklerinin otokontrol manyetik hipertermi uygulamaları için yüksek potansiyele sahip olduğu belirlendi.

Anahtar Kelimeler: otokontrol hipertermi, 1. dereceden Curie faz geçişi, LaFeSiH bileşiği, manyetik nanoparçacıklar.

ACKNOWLEDGEMENTS

I would like to deeply thank my advisor Assoc. Prof. Telem ŞİMŞEK for supporting and guiding me with her knowledge, experience and understanding throughout my research journey. I feel so lucky to meet and work with her, she is the kind of person that creates a positive impact on others' lives and a space for improvement.

I owe SNTG laboratory family, which always felt like a home for me, a big debt of gratitude for all the opportunity and knowledge that they were always ready to offer.

I also thank Assoc. Prof. Ömer GÜLER, Assoc. Prof. Barış AVAR, Asst. Prof. M. Burak KAYNAR, Asst. Prof. Soner ÇAKMAK for their contributions.

And finally, a very special thanks to my family, friends and relatives for all their support that carried me through it all.

CONTENTS

LIST OF FIGURES

LIST OF TABLES

LIST OF SYMBOLS AND ABBRAVIATIONS

Symbols

Å	Angstrom
K	Kelvin
M_s	Saturation Magnetization
T_C	Curie Temperature
T_M	Melting Point

Abbraviations

AMF	Altenating Magnetic Field
BSE	Backscattered Electron
EDS	Energy Dispersive X-Ray Spectroscopy
FM	Ferromagnetic
FOPT	First Order Phase Transition
HSP	Heat Shock Proteins
IEM	Itinerant Electron Metamagnetism
MCE	Magnetocaloric Effect
MHT	Magnetic Hyperthermia Therapy
MNP	Magnetic Nanoparticle
PM	Paramagnetic
SAR	Specific Absorption Rate
SE	Secondary Electron
SEM	Scanning Electron Microscope
SOPT	Second Order Phase Transition

TEM	Transmission Electron Microscope
VSM	Vibrating Sample Magnetometer
XRD	X-Ray Diffraction

1. INTRODUCTION

Recently, cancer has become one of the most widespread diseases, still lacking a definitive cure. The primary cause of cancer lies in the uncontrolled proliferation of damaged cells due to mutations in their DNA. Initially, surgery emerged as the primary method for cancer treatment, followed by the development of other therapies such as radiotherapy and chemotherapy over time. However, while these treatments effectively target cancer cells, they can also influence neighboring healthy cells, resulting in side effects such as fatigue, diarrhea, nausea, and vomiting.

Developing a treatment method that is both curative and non-invasive for cancer patients is crucial. Current therapy methods often lead to the recurrence of cancer tissues. Surgical removal of tumors is employed for small tumors in the early stages [1]. However, the risk of metastases due to vascular invasion remains, especially when tumor resection does not consider the tumor microenvironment. Therefore, in conjunction with this approach, secondary radiation therapy with high doses is often applied to treat cancer patients. Chemotherapy is utilized for treating spreading tumors, delaying cancer progression, and increasing the patient's life expectancy. Given the rapid and uncontrollable growth of cancer cells, chemotherapeutic drugs target fast-growing cells to combat the disease. Unfortunately, these drugs also affect normal fast-growing cells, such as hair follicles, skin cells, oral cells, cells lining the gastrointestinal tract, and cells of the reproductive system. This collateral damage results in side effects such as hair loss, skin problems, oral complications, and gastrointestinal issues.

Preventing cancer recurrence is of paramount importance, driving ongoing research into safer alternative treatments. Promising advancements include gene therapy, immunotherapy, targeted drugs, thermal therapy, and precise imaging methods [2]. Thermal therapy, applied to tumors through photothermal therapy and magnetic hyperthermia therapy (MHT) [3], is a particularly noteworthy avenue. Various methods, such as radio frequencies, ultrasound techniques, microwave irradiation, and infrared laser sources, are employed in photothermal therapy. However, their penetration is limited. Magnetic hyperthermia therapy, on the other hand, benefits from strong tissue penetration ability due to magnetic fields, making tumor depth inconsequential. Moreover, MHT is contactless, enabling a controllable remote treatment [3]. The successful application of MHT for cancer treatment relies on the development of

magnetic nanoparticles (MNPs) with tunable shape and size, good biodistribution, surface modifications, reduced toxicity, and enhanced efficacy capable of bypassing cellular membranes and overcoming drug resistance mechanisms. MNPs serve both therapeutic and diagnostic purposes. Innovative approaches aim to treat cancer safely and effectively, minimizing the impact on healthy cells and reducing adverse side effects. Researchers explore integrating magnetic hyperthermia with gene therapy, immunotherapy, and targeted drug delivery. A study by Chao et al. showcased the synergistic effect of highly magnetic biocompatible polymer-modified iron magnetic nanoparticles in combination with immunotherapy, effectively inhibiting tumor recurrence [4]. Du et al. proposed a strategy for MRI/MPI-guided hyperthermia agents using CREKA-modified magnetic ferrite nanoparticles [5]. Beyond generating heat, MNPs, with added functional groups, can facilitate targeted drug delivery. While MHT can be combined with chemotherapy and radiotherapy for heat-sensitive cancer cells, it can also serve as a monotherapy using sophisticated MNPs to increase tumor temperature above 45-50 °C for a short time, inducing irreversible damage to tumor cells. While only a few clinical centers currently use thermal therapy to treat cancer, ongoing protocols in pre-clinical and approval processes in Europe and the USA underscore its potential. Nanoscale materials, including polymers, dendrimers, lipids, organometallic, carbon-based materials, and various inorganic nanomaterials, are actively studied for their unique structures and properties, aiming for precise and efficient cellular interactions [3].

Despite ongoing developments, there remains a critical need for a mechanism to precisely control temperature in the targeted tissue area, safeguarding nearby healthy cells. To address this, researchers are focusing on auto-controlled magnetic hyperthermia therapy, leveraging the Curie temperature of magnetic materials. For instance, Kawahara et al. achieved auto-controlled heating at 43°C in a subcutaneous tumor using Fe-Al alloy beads and alternating current at 700 W [6]. Their findings demonstrated a reduction in cancer stemness, induction of apoptotic cell deaths, and avoidance of sarcopenia [6]. Achieving an optimal balance between a tunable Curie temperature and strong magnetic properties is crucial for the success of MNPs in auto-controlled MHT applications. The LaFeSi intermetallic compound, with its high saturation magnetization value and tunable Curie temperature, emerges as a promising material for auto-controlled MHT. Auto-controlled MHT, elevating the targeted tissue temperature beyond 45-50 °C, holds the potential to

irreversibly eliminate cancer cells in a short timeframe, bringing us closer to a comprehensive success in the battle against cancer.

2. THEORETICAL INFORMATION

2.1. Magnetic Hyperthermia Therapy

In 1957, Gilchrist et al. pioneered the application of localized hyperthermia therapy principles by heating tumors using magnetic particles and applying an alternating magnetic field (AMF) [7]. The Magnetic Hyperthermia Therapy (MHT) method involves the destruction of cancer cells by targeting or directly injecting a fluid containing magnetic nanoparticles (magnetic nanofluid) into the cancerous tissue. Subsequently, the temperature of the region is elevated by applying an alternating magnetic field, leading to the targeted destruction of cancer cells, as shown in Figure 2.1.

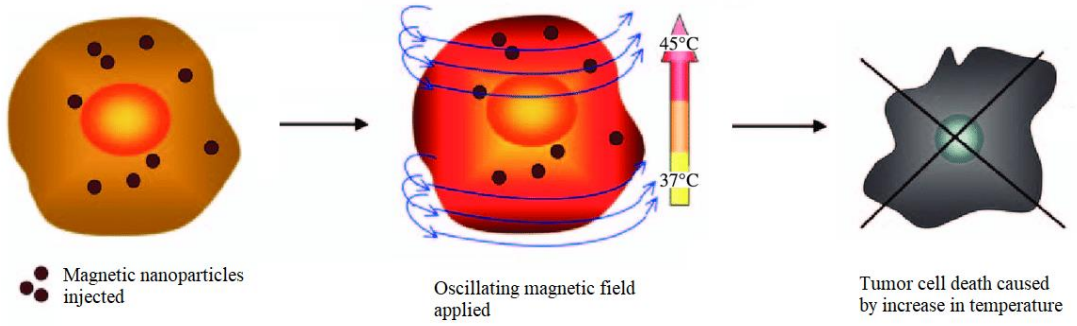

Figure 2.1. Schematic illustration of thermal therapy against cancer, using magnetic nanoparticles [8].

When a ferro/ferrimagnetic material is exposed to an external magnetic field, its magnetic domains undergo changes in orientation and size, leading to the emergence of magnetic poles within the material. Magnetic hysteresis is the term used to describe the situation where the magnetic flux density falls behind the magnetic field strength. The energy retained in magnetic materials when subjected to an external field is known as hysteresis loss, which dissipates as heat during the material's demagnetization process, shown in Figure 2.2-a. In the case of particles small enough to possess a single magnetic domain, they exist in the superparamagnetic phase, where they do not exhibit a hysteresis. In this phase, the particles are randomly oriented due to the thermal effects. When subjected to an external field, the magnetic moment of each single-domain particle aligns.

Upon returning to the equilibrium, the system relaxes in two ways: Néel relaxation and Brownian relaxation (shown in Figure 2.2-b and c). In Néel relaxation, magnetic anisotropy energy is smaller than the thermal energy and the magnetic moment of the particles can freely rotate regardless of the particle's orientation. In such instances, magnetic relaxation occurs without the rotation of the particles. Conversely, in Brownian relaxation, when the magnetic anisotropy energy surpasses the thermal energy, the magnetic moment becomes fixed to the particle. Here, magnetic relaxation takes place with the rotation of the particles [9].

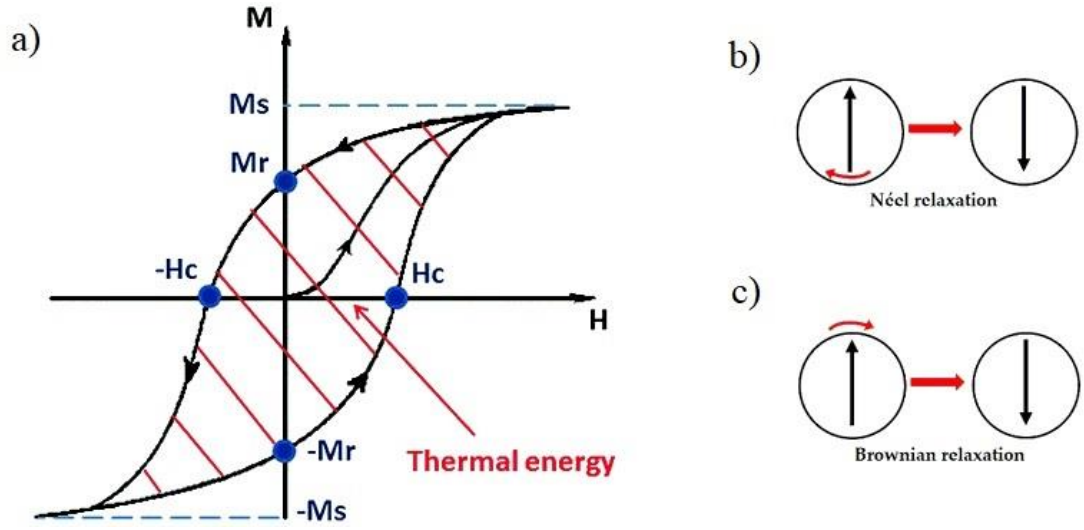

Figure 2.2. Heat generation mechanisms, a) Hysteresis losses, b) Néel relaxation, c) Brownian relaxation [10],[11].

These include saturation magnetization, magnetic anisotropy constant, relaxation time, viscosity of the liquid media, magnetic field strength, and frequency. Structural properties such as particle uniformity, shape, and diameter, as well as modifications, core/shell compositions, and sizes can significantly influence the magnetic properties. Additionally, factors such as injection volume, dosage, homogeneous distribution within the target area, biocompatibility, prevention of particle aggregation, and resistance against oxidation are equally important in ensuring the effectiveness of the treatment. One of the main advantages of MHT is its local and noninvasive nature. Cancer cells, because of their immature vasculature, are more sensitive to heat, making them susceptible to this treatment. In contrast, healthy tissues, which have normal thermoregulation functions, are more resistant to heat, minimizing damage to non-cancerous cells during the therapy [13]. These make MHT a safer way compared to other methods, for treating cancer. The heating efficiency of MNPs is measured by specific absorption rate (SAR):

$$SAR = \frac{C}{m_{mag}}\left(\frac{\Delta T}{\Delta t}\right) \qquad \text{Eq.1.}$$

Here C is the heat capacity of the liquid (J/K), m is the mass of the magnetic nanoparticles (in kg) and $\Delta T/\Delta t$ is the initial slope of temperature rise as a function of time (in $°Cs^{-1}$), when the AMF is turned on. The unit of SAR, measured in watts per kilogram (W/kg), indicates the rate at which electromagnetic energy is absorbed by a unit mass of a substance.

2.2. Auto-Control Hyperthermia

Hyperthermia can be employed in conjunction with radiation and chemotherapeutics. When used to enhance the sensitivity of tumors to radiation and chemotherapeutics, the temperature of the targeted region should ideally be maintained within the range of 40 – 45 °C [13]. When hyperthermia is utilized as a monotherapy for thermal ablation, the temperature must be higher than 50 °C for direct tumor cell death by coagulative necrosis within a short time [13],[14]. Indeed, controlling the temperature within the targeted tissue, to protect the healthy cells nearby, poses a challenge for improving MHT applications. Thus, utilizing magnetic nanoparticles with a Curie temperature around 50

°C or higher can offer a potential solution for an auto-controlled hyperthermia mechanism, to treat cancer both non-invasely and safely.

At the Curie temperature (T_C), ferro/ferrimagnetic (FM/FI) materials becomes paramagnetic (PM). At this critical temperature, the thermal energy overcomes the exchange energy, causing the magnetic domains to align randomly, and the material loses its permanent magnetism. As a consequent of magnetic domain alignments being independent from the external magnetic force, heat generations that arise during the alignment with the external field direction does not occur any longer. PM materials are weakly attracted to an external magnetic field and require a strong field to align with its direction. Consequently, they generate much less heat under an AMF compared to FM/FI materials.

FM/FI to paramagnetic PM transitions are classified into two types based on their behavior: first-order phase transitions (FOPT) and second-order phase transitions (SOPT). FOPT occurs abruptly, while SOPT happens gradually as shown in Figure 2.3. In the context of a magnetic material undergoing a first-order Curie transition at approximately 50 ºC, the shift from FM/FI to PM behavior is abrupt. Consequently, in applications like magnetic hyperthermia, the material's heating mechanism quickly ceases once the surrounding temperature equals the Curie point, which is called auto-control hyperthermia or self-controlled hyperthermia.

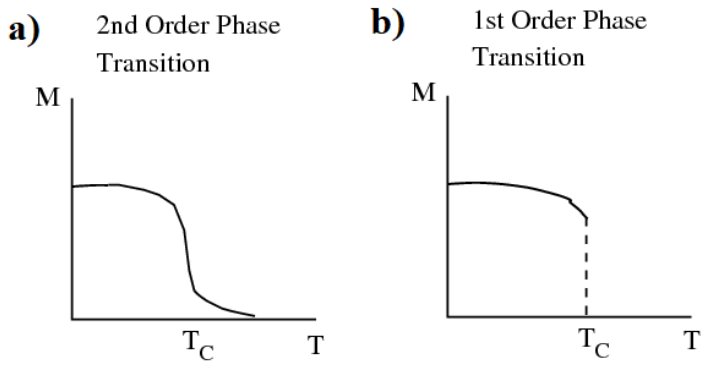

Figure 2.3. a) SOPT and b) FOPT behaviours [15].

For auto-control MHT studies, Hejase et al. chemically synthesized MnZnFeO MNPs with a TC of 56 °C and saturation magnetization of 23 emu/g [16]. Prasad et al. successfully synthesized ferromagnetic $La_{0.73}Sr_{0.27}MnO_3$ nanoparticles exhibiting a saturation magnetization of approximately 38 emu/g (measured at 20 kOe) and T_C of 45 °C, ensuring prevention of overheating. These nanoparticles demonstrated SAR value of

15.6 W/g in the presence of 150 Oe field strengtheand a frequency of 425 kHz [17]. Kuznetsov et al. showcased the potential of auto-controlled heating in CuNi nanoparticles [18]. In their study, Kuznetsov et al. enhanced the uniformity of the particles by utilizing magnetic separation and investigated the impact of mechanical treatment on the magnetic transition. They reported heating effect of nanoparticles under 410 kHz applied field, resulting in a temperature increase to 43 °C.

Meanwhile, Akin et al. conducted research on arc-melted $Ni_{(1-x)}Cr_{(x)}$ particles with varying compositions for localized auto-control hyperthermia treatment of cancer. They achieved a Curie temperature of 44 °C (317 K) successfully by adjusting the chromium concentration to 5.63 wt%. [19]. In Mohite's study, $ZnGd_xFe_{(2-x)}O_4$ nanoparticles with an average size of 200 nm, were synthesized using co-precipitation method. These nanoparticles exhibited a Curie temperature of 41 °C (314 K) when x = 0.02. This finding is significant as it makes these nanoparticles suitable for auto-control hyperthermia applications [20].

Several studies have explored the control of local treatment temperature in MHT through computational estimation methods involving external factor modulations. These methods often utilize advanced simulations and computational models to predict and optimize the distribution of heat within the targeted tissues. By modulating external factors such as magnetic field strength, frequency, and nanoparticle properties, researchers aim to achieve precise temperature control during hyperthermic treatments. This computational approach is important for enhancing the effectiveness and safety of MHT procedures [21-24]. Nevertheless, the implementation of automated temperature control using these methods in clinical hyperthermia applications is still an ongoing research topic.

In conclusion, despite the advancements in auto-controlled hyperthermia research, achieving a rapid and effective monotherapy requires the development of a material capable of providing permanent treatment safely and swiftly. LaFeSi, with its notable saturation magnetization value, holds the potential to fulfill such a role, as its Curie point can be finely adjusted by modifying the quantity of light elements incorporated into its structure.

2.3. LaFeSi Compound

The combination of unique chemical composition, high magnetization, biocompatibility, and thermal stability makes LaFeSiH nanoparticles as promising candidates for MHT applications. These nanoparticles have the potential to revolutionize cancer therapy by offering precise and effective localized heating and auto-control hyperthermia properties. $LaFe_{(13-x)}Si_{(x)}$ materials exhibit low hysteresis losses due to their soft magnetic character. They exhibit a lower toxicity profile when compared to materials based on Ni, Mn, and Gd that have been explored in self-comtrolled MHT studies. Moreover, since their constituent elements are abundant, these materials are less costly. Ternary $La(FeSi)_{13}$ compounds can have different crystal structures owing to their compositional ratios [25]. $LaFe_{(13-x)}Si_{(x)}$ crystallizes in the face-centered cubic (fcc) structure in the range of $1 \leq x \leq 2.6$, as shown in Figure 2.4. For values of x between 3.2 and 5, the compound forms a tetragonal structure at room temperature [26],[27]. However it exhibits a two-phase mixture in the range of $2.6 \leq x \leq 3.2$ [26].

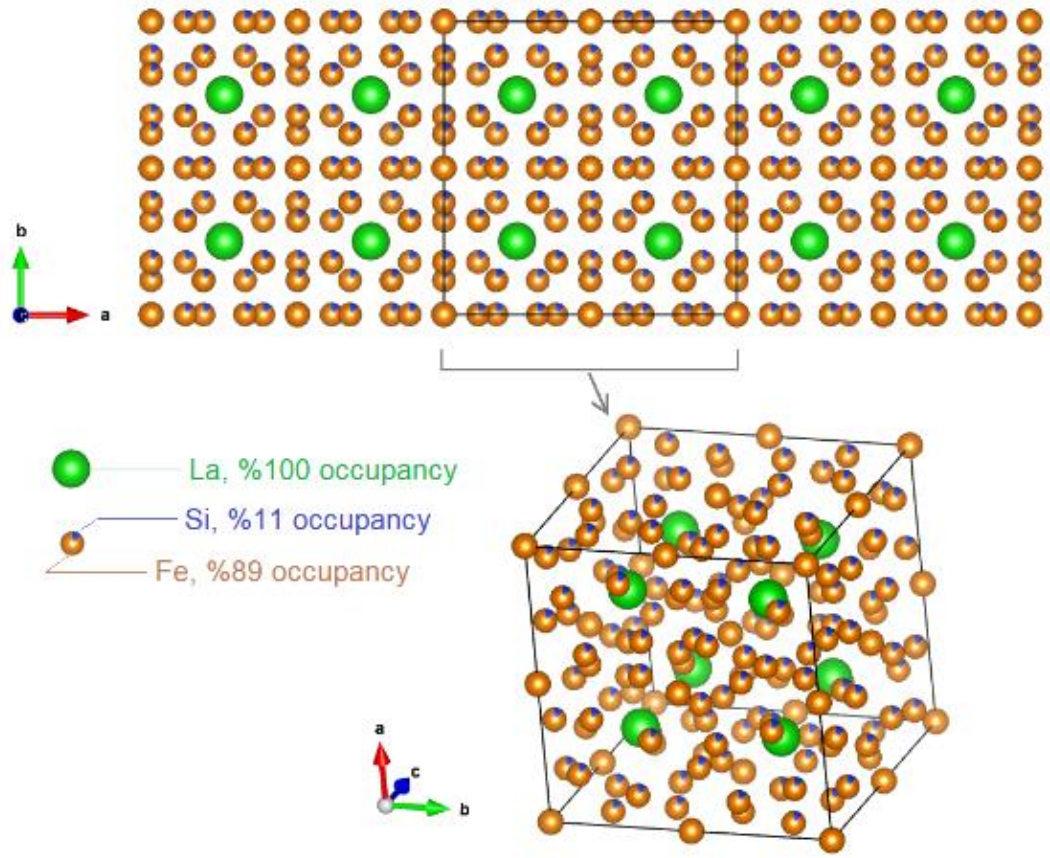

Figure 2.4. Crystal structure of $NaZn_{13}$-type cubic $LaFe_{11.57}Si_{1.43}$ created in VESTA.

Achieving a homogeneous fcc $NaZn_{13}$-type LaFeSi structure necessitates extended periods of heat treatment, often ranging from 10 to 40 days [28]. However, the presence of body-centered cubic (bcc) α-Fe impurity phase precipitates in the compound, depending upon the specific production conditions [29]. This occurrence can be attributed to the incomplete peritectic reaction, requiring an extended heat treatment duration to facilitate the comprehensive solid reaction necessary for the formation of the 1:13 phase [30].

There are various methods to synthesize LaFeSi compounds. Most popular approach involves initial compounding through the arc-melting method, followed by annealing to achieve homogenization. The compound is sealed in a quartz ampoule under high vacuum conditions and then quenched rapidly by immersing it in ice water [31]. Another method is ball milling the arc-melted LaSi ingot with Fe and Si powder. Subsequently, the as-milled compounds exposed to annealing in silica ampoule that is sealed under Ar atmosphere [32].

Figure 2.5. shows LaFeSi ternary phase diagram at 25 °C. τ1a denotes cubic $NaZn_{13}$-type structure, τ1b denotes the tetragonal structure, τ2 denotes Al_4Ba-type tetragonal structure, τ3 denotes tetragonal $LaFe_{1.3}Si_{2.7}$ structure, τ4 denotes Cu_2Sb-type tetragonal structure, and τ5 denotes the hexagonal AlB_2-type structure [25].

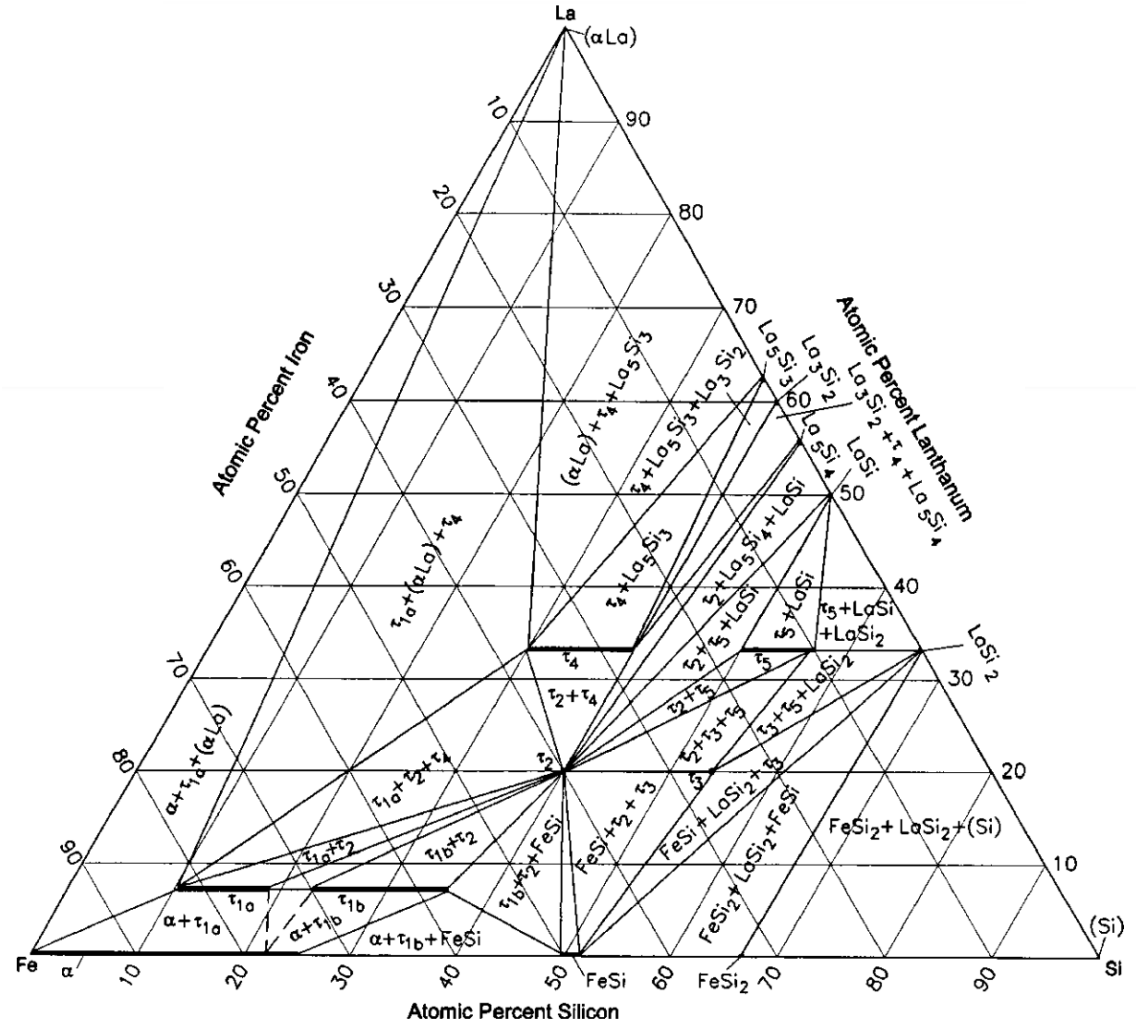

Figure 2.5. Isothermal section at 25 °C of LaFeSi ternary phase diagram [25].

The τ1 phase, with its low Si concentration, displays a significant magnetocaloric effect (MCE) across a wide temperature range. Conversely, the τ2 phase possesses a substantial magnetocrystalline anisotropy, making it resistant to demagnetization, which results in high magnetic stability [31]. The 1:13 compound with a low Si content (approximately $1.2 < x < 1.8$) exhibits an itinerant electron metamagnetic transition (IEMT) above its T_C. During this transition, there is a sharp change in magnetization, indicating a significant alteration in the material's magnetic properties [33]. In $La(Fe_{(13-x)}Si_{(x)})_{13}$ compounds, the entropy change is more significant for smaller x values, indicating a characteristic of

FOPT. As the Si content increases, the first-order character of the transition diminishes, leading to a decrease in the entropy change, as observed in the study by Valérie Paul-Boncour [34].

The $LaFe_{(13-x)}Si_{(x)}$ compound with x=1.5 exhibits a Curie point around 198 K [26]. Indeed, the Curie temperature of compound can vary based on the Si content. Moreover, the Curie temperature may also be influenced by the presence of other substitutional elements like manganese (Mn), cobalt (Co), and the insertion of light atoms such as hydrogen (H) and carbon (C) [35] or B, N [36],[37]. These substitutions and insertions can modify the magnetic properties, altering the Curie temperature and making these materials suitable for specific applications.

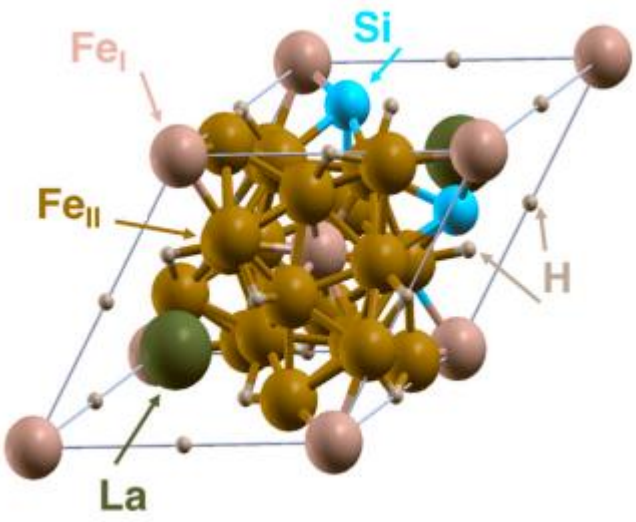

Figure 2.6. Primitive cell of fully hydrogenated $LaFe_{11.5}Si_{1.5}H_3$ [38].

The insertion of carbon (C), substitution with cobalt (Co), or the addition of boron (B) in $La(FeSi)_{13}$ intermetallic compounds can lead to a decrease in the entropy change, weakening order FOPT at T_C [36],[34]. Due to the larger size of nitrogen (N) atoms compared to H atoms, nitrogenation of $LaFe_{13-x}Si_x$ leads to a more substantial lattice expansion. Conversely, the addition of a similar molar amount of H results in a greater increase in the T_C with a smaller expansion in the lattice parameter (Figure 2.6) [39].
LaFeSi compounds can be hydrogenated through thermal or mechanical methods. Mandal et al. showed that the compound can be successfully hydrogenated by heating in the presence of 5 bar H_2 [40]. Additionally, the compound can be hydrogenated through

mechanical milling under H_2 atmosphere [40]. Bez et al. hydrogenated $La(FeSi)_{13}$ compound via the Hydrogen-Decrepitation-Sintering-Hydrogenation process [41].

2.4. Motivation

The motivation of this work is employing physical synthesis methods for the production of LaFeSiH particles to elevate its Curie temperature to the targeted 320 K, suitable for magnetic auto-control hyperthermia therapy. This goal is pursued by introducing hydrogen, a highly lightweight element capable of diffusing into the material's vacancies intersititially, thereby altering its magnetic properties through magnetovolume effect. Subsequent chapters will give a detailed information on the experimental procedure employed in this study.

3. EXPERIMENTAL SECTION

3.1. Synthesizing Methods

Bulk LaFeSi ingots are first produced by arc-melting, and thermal treated after encapsulation in quartz tubes. Homogenized ingots are hydrogenated with two different ways; using Sievert type apparatus followed by vacuum heating, and ball-milling.

Detailed informations are covered in Section 4 and 5.

3.1.1. Arc-melting

Arc melteing has been known for metal melting and compounding using plasma. The application is based on plasma heating generated by electric arc discharge. Vacuum arc-melting is a suitable technique for non-contaminating homogeneous compounding. Main components of an arc-melter system are furnace chamber, electrode, plate, inert gas system, vacuum system, power supply and water cooling system (Figure 3.1). In the vacuum chamber the electric arc is generated via a tungsten electrode. Argon gas is used for facilitating the formation of the electric arc. Metals to be melted are placed on copper crucible and the chamber is vacuumed by pumping. The crucible is water-cooled to prevent copper contamination to the target metals. To avoid oxidation, titanium pieces as oxygen-getters are kept on the crucible to be melted before the target metals.

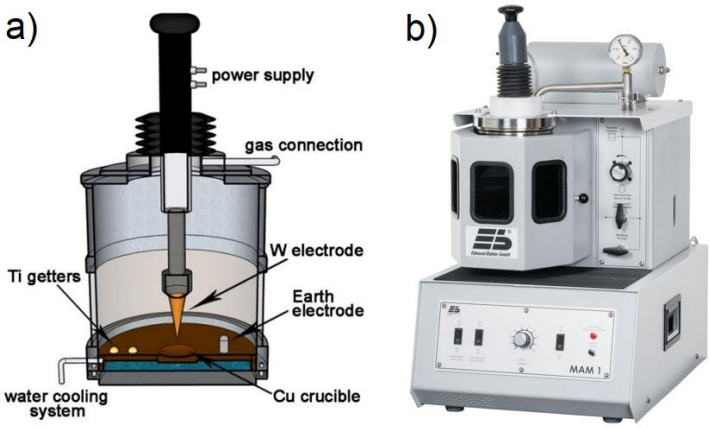

Figure 3.1. a) Schematic of arc-melter [42], b) Edmund Buehler MAM-1 arc-melter [43].

3.1.2. Encapsulation

Encapsuling of the sample to quartz tubes is a technique used to protect the sample from oxidation during annealing at high temperatures to increase homogeneity. Vacuum quartz sealing system set-up consists of argon, oxygen and hydrogen gas cylinder tanks (Figure 3.2-a), a turbomolecular pump (Figure 3.2-b), torch with a nozzle hole diameter of 0.5-1 mm (Figure 3.2-c), quartz tube integrated to the pumping system with vacuum hoses and valves.

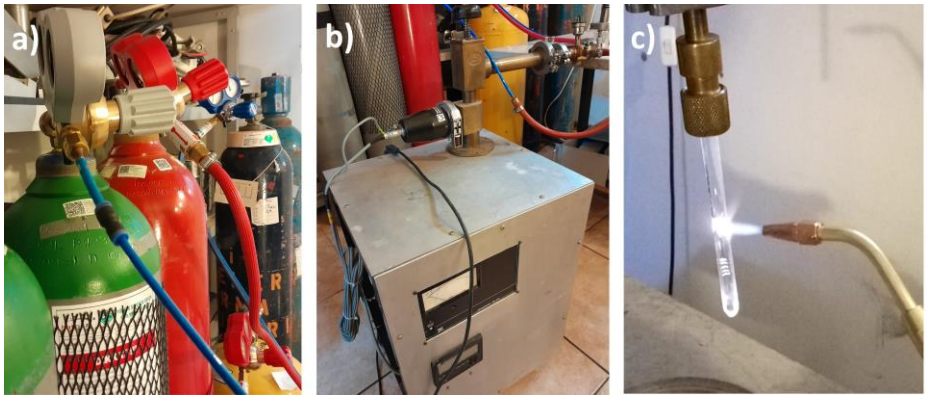

Figure 3.2. Quartz sealing system a) argon, hydrogen and oxygen gases, b) turbo-molecular pump, c) encapsulation process.

3.1.3. Heat Treatment

Heat treatment is a process used to alter or enhance the physical properties of materials. Thermally activated atoms start to move in the crystal leading to changes in the physical properties of the material such as ductility, hardness, homogeneity, crystallinity and strength. For this process, furnaces are used that generally contains thermocouple, temperature controller, pumps and gas flow system. In this work, Stuart Scientific Box Furnace is used for the homogenization of the samples sealed in quartz tubes (Figure 3.3a,b). For the reverse hydrogen diffusion in $La(FeSi)_{13}H_y$ powder samples, Thermo Scientific Lindberg Blue M model tube furnace is used (Figure 3.4a,b).

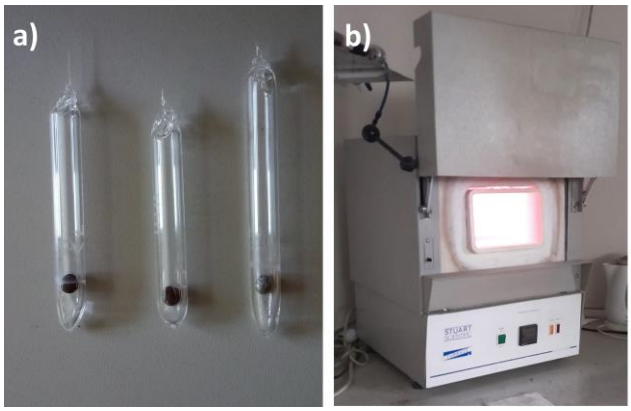

Figure 3.3. a) Ingots sealed in quartz ampoules, b) furnace used for heat treatment.

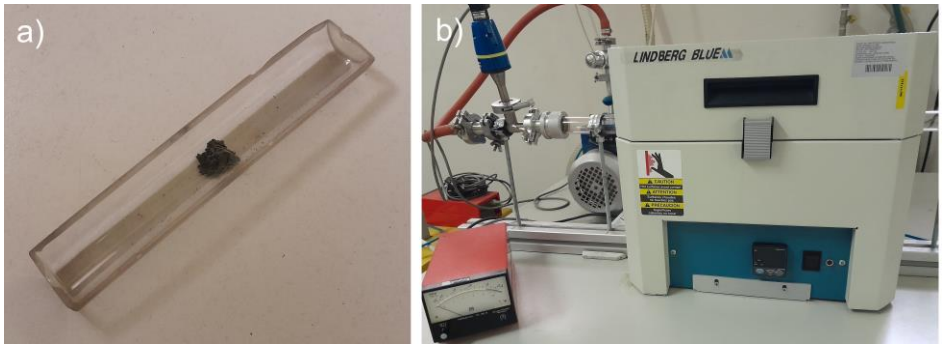

Figure 3.4. a) Sample in the quartz crucible, b) tube furnace.

3.1.4. Mechanical Milling

In this work, milling is conducted by using a planetary ball-mill, as depicted in Figure 3.5-a. In the experiments, locked grinding jar serves as the grinding pot, which contains milling balls (Figure 3.5-b). In this technique, the mill rotates around its own axis while the jars containing grinding media and the material to be ground rotate around a common center. The rotational movement of the jars and the milling balls inside them result in the effective grinding of the materials. The outcomes of the milling heavily depend on vial volume, size of the balls, weight ratio of ball and sample, rotation speed, and time.

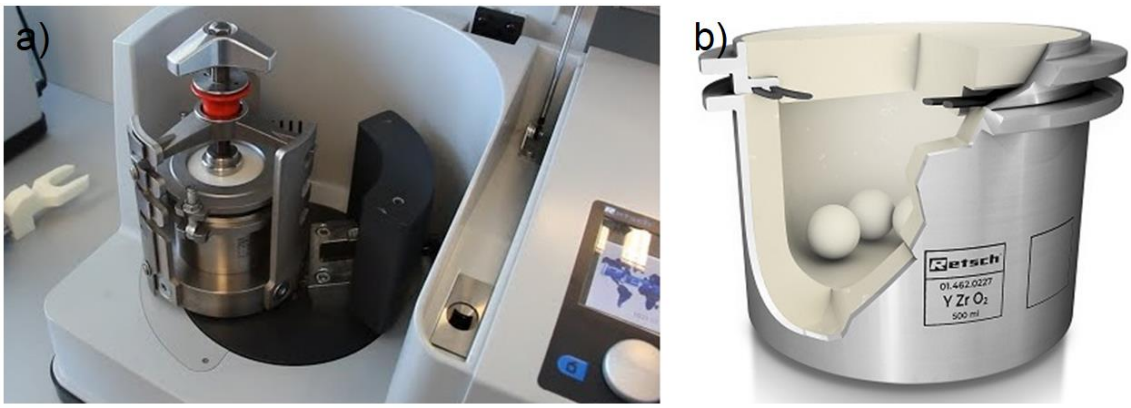

Figure 3.5. a) Retsch planetary ball-mill, b) grinding jar [44].

3.1.5. Volumetric Sievert-type Apparatus

Sievert's apparatus is a specialized equipment used for studying hydrogen absorption/desorption kinetics and determining pressure–composition isotherm (PCT) diagrams of metal–hydrides. It is designed to maintain constant pressure within the reaction chamber during these processes. It is comprised of a gas manifold connected to a calibrated gas reservoir volume (reference reservoir) by a sequence of pipes and valves (Figure 3.6 a-c). [45]. The sample reservoir is filled with the sample, and the starting pressure is recorded. In order to do absorption, the sorption gas is pumped into the reservoir to a pressure that is preset above the sample volume's initial pressure. Gas is permitted to equilibrate between the two reservoir volumes when the isolation valve between them is opened [46]. The system volumes and the pre-known beginning gas pressures can be used to calculate the amounts of gas that have been absorbed or desorbed [47].The z factor (gas compressibility) in the real gas equation is approximately 1 at atmospheric conditions and well-known ideal gas equation can be used as:

$$PV=nRT \qquad \text{Eq.2.}$$

Where P is the pressure, V is volume, n is the total number of moles of the sorption-gas in the reservoirs, R is the gas constant, T is the temperature.

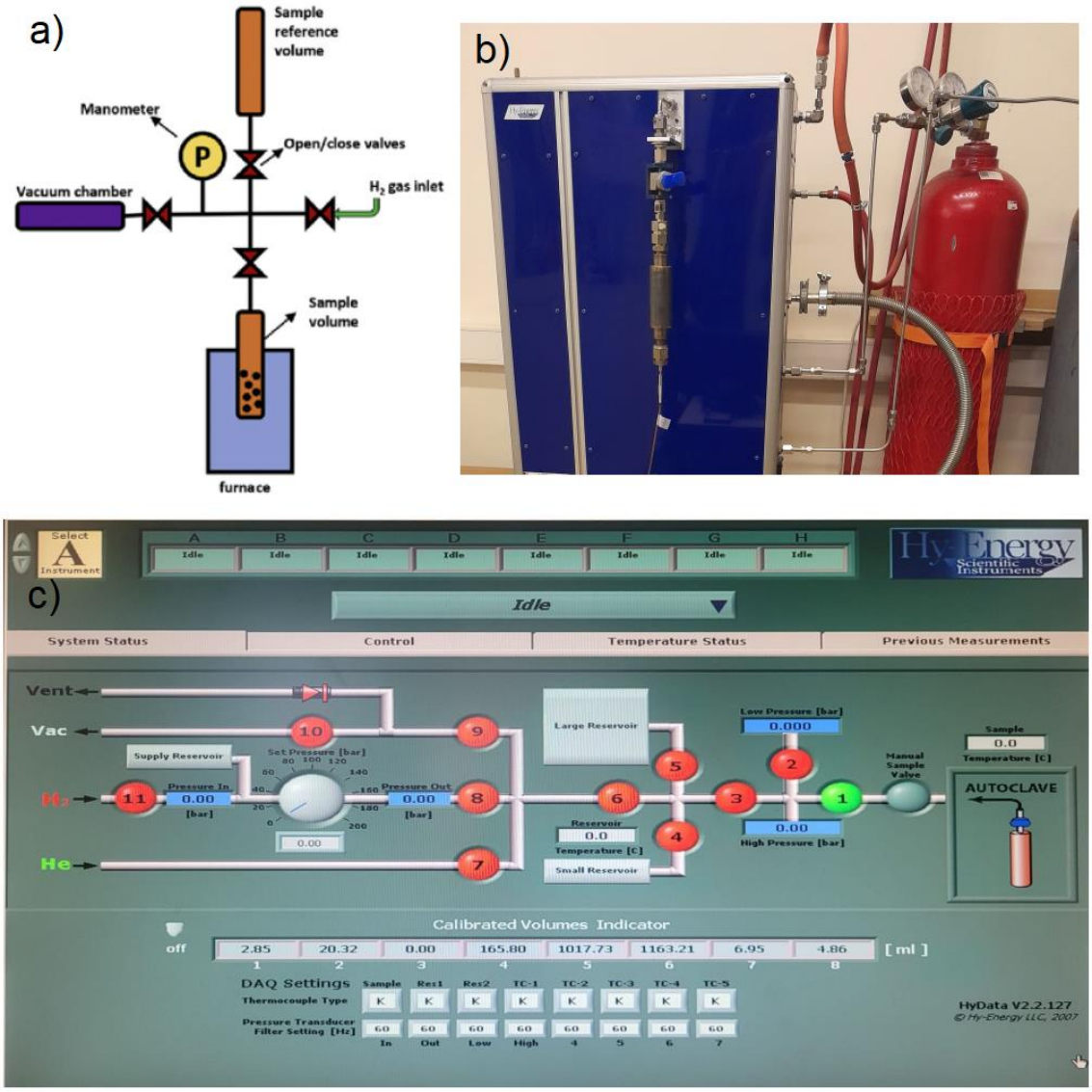

Figure 3.6. a) Block diagram of the Sievert-type apparatus [48], b) HyEnergy PctPro-2000 Sievert-type apparatus, c) Control panel of the HyData software

3.2. Characterization Methods

Samples are subjected to comprehensive structural, elemental, magnetic and magnetothermal characterizations before and after the hydrogenation steps. Structural analysis of the samples are made by using X-ray Diffraction, Scanning Electron Microscopy and Energy Dispersive X-ray Spectroscopy methods. Magnetic and magneto-thermal properties are investigated using Vibrating Sample Magnetometer and Magneto-Thermal Measurement System.

3.2.1. X-Ray Diffraction

X-ray diffraction (XRD) is a powerful technique used for analyzing the crystal structure of materials. It is based on the principle of X-ray scattering, where X-rays are directed at a crystalline sample, and the resulting diffraction pattern provides information about the arrangement of atoms in the material. The resulting diffraction pattern, formed when the Bragg's Law is satisfied, offers valuable insights into the arrangement of atoms within the material. The angle of incidence, X-ray wavelength, and the interplanar spacing between crystal lattice planes are all related by Bragg's Law. This relationship is crucial for understanding how X-rays interact with the crystal structure. Given that the atomic distances between bonded atoms in ordered solids are typically a few ångströms, and the wavelength of X-rays falls within the range of 0.01-10 nm, XRD is well-suited for probing the intricate details of crystal arrangements. Different crystal structures in solid materials yield distinct diffraction patterns when interacting with X-rays. By analyzing these patterns, the structure of solids can be identified.

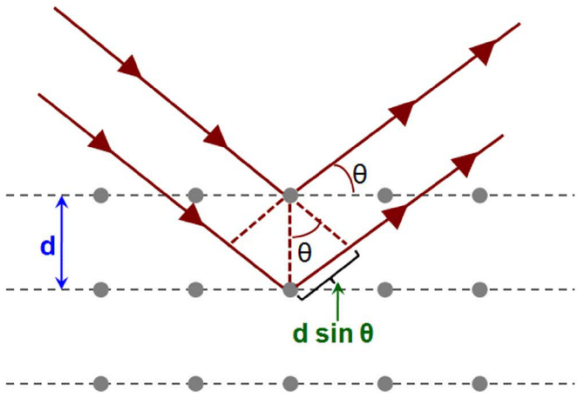

Figure 3.7. Illustration of Bragg condition [49].

Condition for the constructive interference is satisfied when diffracted rays are in phase. Thus path difference between two beams will be equal to an integer number (n) of the incident wavelength (λ). As d is the distance between the parallel atomic planes, and θ is the incident angle in Figure 3.7, path difference is equal to 2dsinθ. Thus, Bragg's equation is represented as

$$n\lambda = 2d\sin\theta \qquad \text{Eq.3.}$$

XRD analysis serves as a powerful tool for obtaining crucial insights into a material's characteristics, such as crystallinity of the sample, determination of phase compositions, unit cell parameters, crystallite size and lattice strain. XRD measurements of the samples are done using Malvern PANalytical Empyrean powder diffractometer (CuK-α radiation, 1.54 Å) (Figure 3.8.).

Figure 3.8. Malvern Panalytical Empyrean XRD instrument [50].

3.2.2. Scanning Electron Microscopy (SEM)

Scanning Electron Microscopy (SEM) is a technique used for detailed imaging and analysis of the surfaces of solid specimens. The Scanning Electron Microscope (SEM), depicted in Figure 3.9, comprises a microscope column, a controlling console, and a vacuum system. The control unit allows for adjustments necessary for imaging purposes. In the microscope column, an electron beam is generated by an electron gun, then accelerated, focused, and scanned by electromagnetic lenses and apertures, all within a vacuum environment. Interaction of the electron beam with the sample surface results in the inelastic scattering of electrons (secondary electrons) or elastic scattering (backscattered electrons). The imaging mode that detects secondary electrons (SE) is suitable for topographic analysis, providing information about surface features. Conver-

sely, backscattered electron (BSE) patterns are useful for phase analysis, as BSEs originate from deeper regions of the sample. The contrast in the BSE image is influenced by the atomic number of the elements, with higher Z numbers leading to increased electron scattering. It is essential for the sample in SEM analysis to be electrically conductive or coated with a conductive material. This requirement ensures proper electron beam interaction and imaging capabilities.

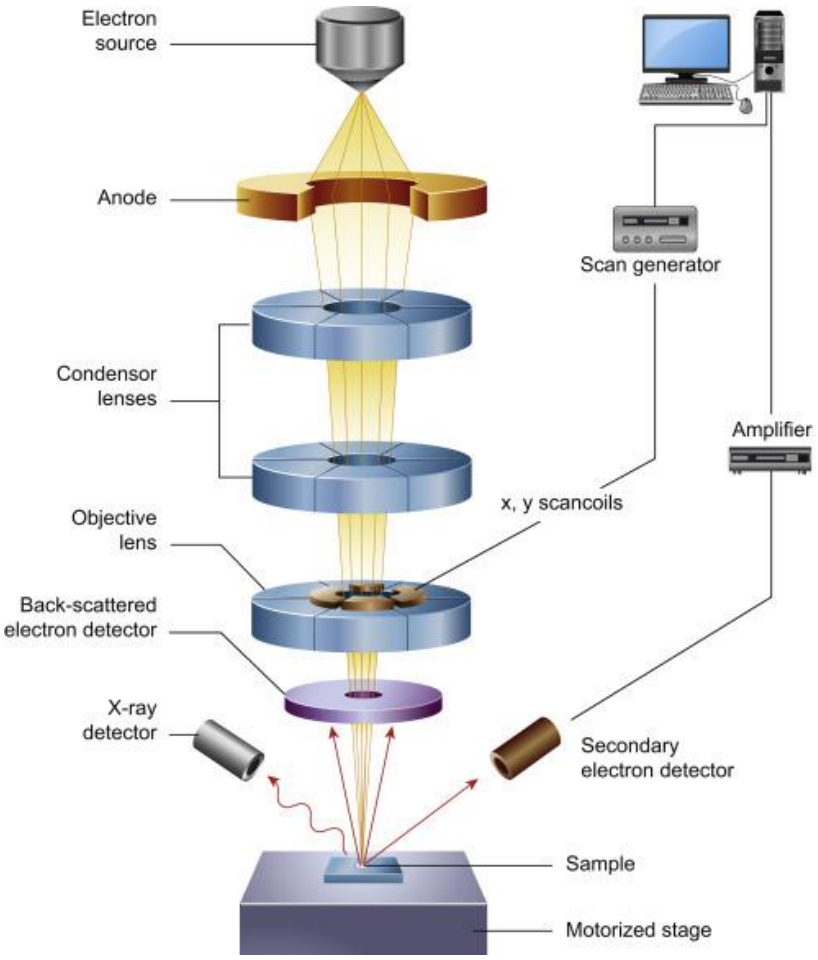

Figure 3.9. Schema for SEM system [51].

Figure 3.10. Tescan GAIA3 Scanning Electron Microscope [52].

SEM images of the samples are taken by Tescan GAIA3 SEM instrument (Figure 3.10), for morphology and particle size analysis. For backscatter images, bulk LaFeSi sample pieces were embedded in a resine, and the surface was grinded, then polished in three stages, by LaboPol-35 Struers grinding and polishing equipment.

3.2.3. Vibrating Sample Magnetometer (VSM)

A Vibrating Sample Magnetometer (VSM) is a versatile instrument to study the magnetic properties of materials, providing insights into how a solid's magnetic behavior changes with external magnetic fields or temperature variations. This technique yields valuable information such as magnetic phases, phase transitions, remanent and saturation magnetization, and coercivity. The main components of a typical VSM system in Figure 3.11.

The working principle of VSM is based on Faraday's Law of induction [53]. A sample is put into a constant external field that will magnetize the sample by aligning the magnetic domains, or the individual magnetic spins, with the field. Resulting magnetic dipole moment of the sample creates a magnetic field that changes as the sample is vibrated. This field changing in time will induce a current that is proportional to the magnetization

of the sample [54]. Thus, magnetization of the sample will be determined based on the sensed current in the coils (Figure 3.11).

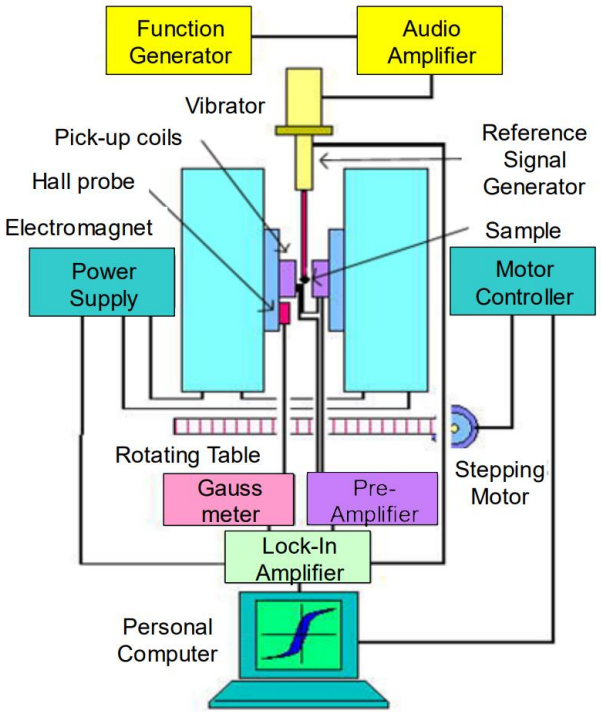

Figure 3.11. Schematic of a VSM set-up [55].

In the experiments, the VSM option of Quantum Design Physical Properties Measurement System is used, as shown in Figure 3.12. Magnetization of the powdered samples as a function of external applied field and as a function of temperature are measured.

Figure 3.12. Quantum Design Physical Properties Measurement System

3.2.4. Magneto-Thermal Measurement

The Specific Absorption Rate (SAR), serving as a measure of the comparative effectiveness of different materials for Magnetic Hyperthermia (MHT), can be experimentally determined using the system depicted in Figure 3.13-a. The measurement system comprises an induction heating system, a circulating water chiller system, a a fiber optic temperature sensor, and a computer interface (Figure 3.14). Within the induction heater's coil (Ambrell EasyHeat LI) (Figure 3.13-b), an oscillating magnetic field is generated. The solution containing Magnetic Nanoparticles (MNPs) within an Eppendorf tube is positioned at the center of the solenoid coil. A fiber optic sensor is immersed in the solution, measuring the heating behavior of the MNPs in the liquid under an Alternating Magnetic Field (AMF). The $\Delta T/\Delta t$ term in the SAR equation, crucial for the experimental calculation of the extrinsic heating power parameter, is determined from temperature measurements over time. This is achieved by extracting the initial slope of the curve during the first 10-100 seconds, where the temperature exhibits a linear behavior due to the minimal impact of thermal losses.[56]. In the measurements, AMF is 26 kA/m with a frequency of 300 kHz ($H_0.f$=7.9 A/(m.s)).

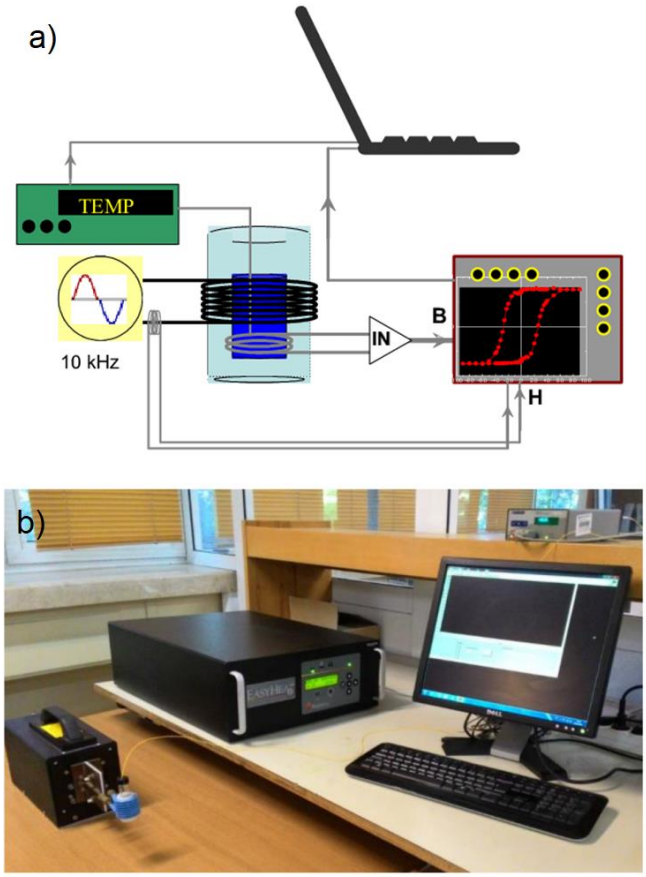

Figure 3.13. a) Schematic of magneto-thermal measurement system [57], b) Ambrell EasyHeat LI induction heater, coil, fiber optic temperature sensor and computer

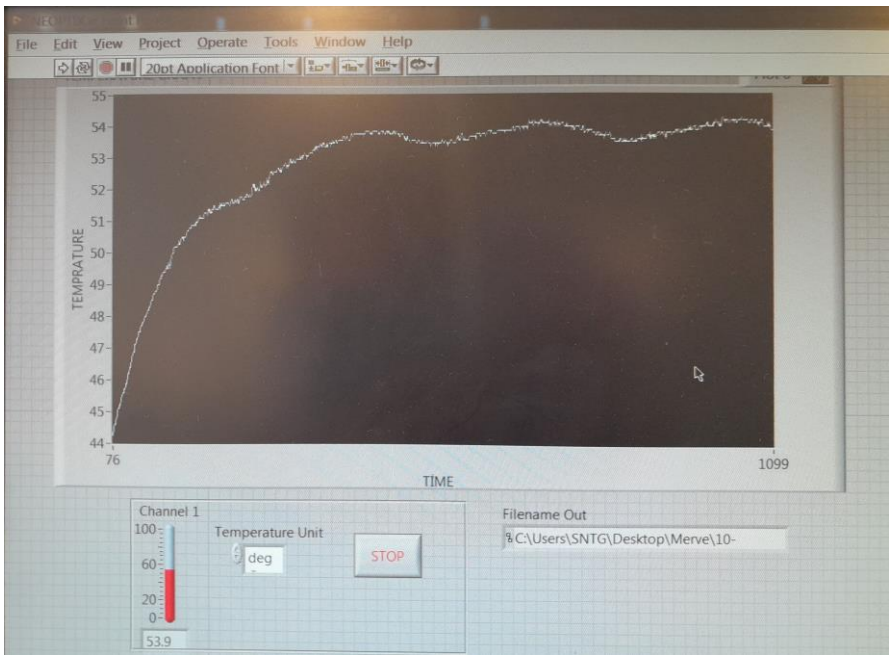

Figure 3.14. LabView interface for the magneto-thermal measuremet system.

4. BULK LAFESI COMPOUND

In this section, synthesis and characterization steps of the bulk LaFeSi samples are given in detail.

4.1. Production of Bulk LaFeSi Ingots

Here, melting and following homogenization process of bulk LaFeSi samples will be explained.

4.1.1. Production of LaFeSi Ingots by Arc-Melting

Elemental lanthanum pieces, iron and silicon powders (Sigma-Aldrich) with purity of 99.9% are used to produce the parent (base) compounds. The starting materials are kept in a glove-box filled with inert Ar gas. Calculated amounts of the elements to form 0.5 g of $LaFe_{11.57}Si_{1.43}$ compound (0.3915 g Fe, 0.0926 g La, 0.0243 g Si) are measured in the glove-box. 10 wt.% excess lanthanum was added in order to compensate for the loss of lanthanum in melting process. The precursors are melted via Edward Buehler MAM-1 model mini arc-melter system (Figure 3.1-b). The arc-melted ingots are remelted three times after flipping to increase the homogeneity (Figure 4.1). The weight of the as-melted ingot is measured, after every melting step. As-produced ingots are stored in glove-box.

Figure 4.1. Arc-melted LaFeSi ingot.

4.1.2. Homogenization of LaFeSi Ingots

The arc-melted ingots are sealed in quartz ampoules for homogenization. First the ampoules are evacuated by purging and pumping three times with non-reactive inert Ar gas and turbomolecular pump. An oxy-hydrogen torch is used for the sealing process. Ampoules are tested in ethanol to ensure the vacuum sealing. The sealed ampoules are

annealed at 1000 °C for 4, 7 and 10 days durations in a box furnace, to achieve the homogeneous structure. After annealing process, the ampoules are rapidly quenched in ice water, for the nucleation competition between α-Fe impurity phase and main $La(FeSi)_{13}$ phase [58].

4.2. Structural Properties of Bulk LaFeSi

4.2.1. XRD Analysis of Bulk LaFeSi

Figure 4.2 shows the XRD patterns of the bulk LaFeSi samples annealed for 4, 7 and 10 days for homogenization. The desired $NaZn_{13}$-type cubic structure is formed as main phase in all three sample. The calculated physical parameters after Rietveld refinements are summarized in Table 4.1. The secondary α-Fe phase fraction of the samples are calculated as 35.2, 34.1 and 5.6, respectively. Morever the SiO_2 phase is observed in the sample anneled for 4 days whereas 7 and 10 days anneled samples don't contain the oxide phase. Thus long-term heat treatment facilitates the desired compound structure and the impurity content decreases significantly with the increasing annealing time. Results also show that excess La is needed to compensate the La losses through evaporation, since melting point of La is lower than Fe and Si (T_M(Fe)=1538 °C, T_M(Si)=1410 °C, T_M(La)=920 °C). The bulk sample annealed for 10 days contains 94.4% $La(FeSi)_{13}$ and 5.6% Fe impurity which originates from peritectic solidification of the compound [58]. As heat treatment temperature and time increased, the homogeinity of the ingots is improved. Due to its high homogeneity and low α-Fe content, sample annealed for 10 days is chosen as parent sample for the hydrogenation processes in the remaining part of the work.

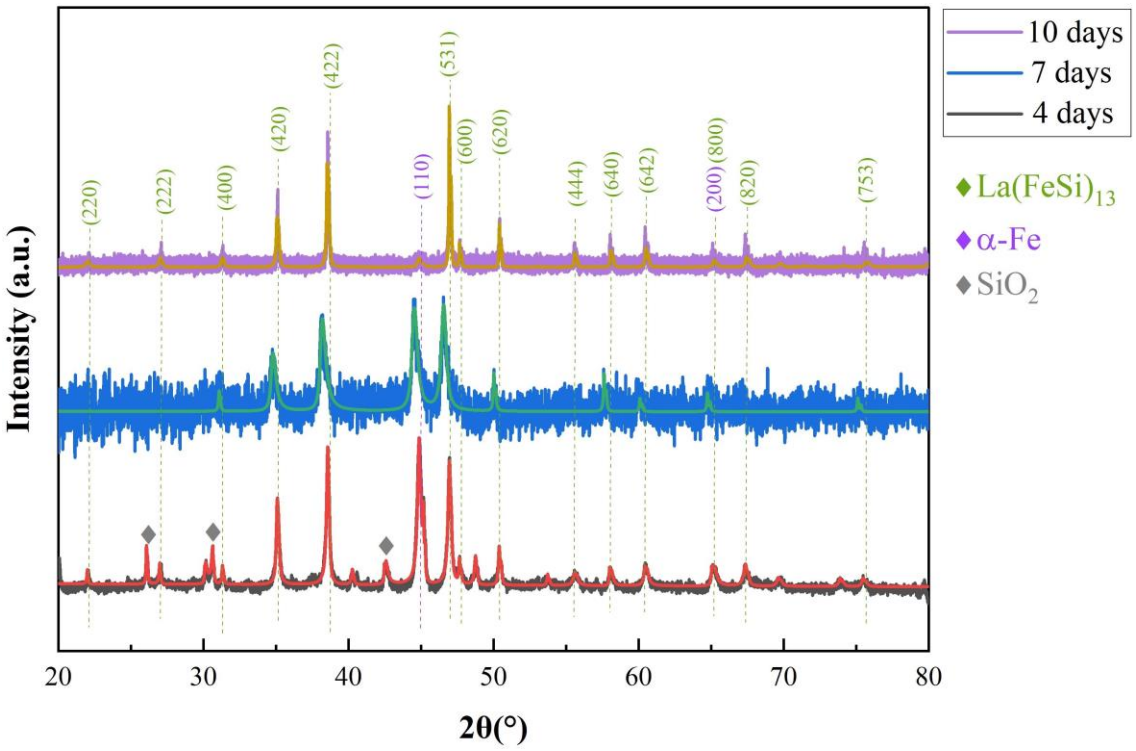

Figure 4.2. XRD patterns of bulk LaFeSi compounds homogenezied for 4 to 10 days.

Table 4.1. XRD results of LaFeSi samples homogenezied for 4 to 10 days.

	$La(FeSi)_{13}$ phase fraction (wt%)	Lattice parameter (Å)	SiO_2 fraction (wt%)	α-Fe (wt%)
4 days	54.1±0.7	11.4562±0.0003	10.7±0.7	35.2±0.4
7 days	65.9±0.5	11.5040±0.0004	-	34.1±0.5
10 days	94.4±0.4	11.4483±0.0005	-	5.6±0.4

4.2.2. SEM and EDS Analysis of Bulk LaFeSi

The morphology and structure of the $La(FeSi)_{13}$ parent sample are shown in in Figure 4.3. The elemental compositions are identified by EDS analysis (Figure 4.4). In mapping images

Fe is represented with green, Si in yellow and La in red. Average La, Fe and Si atomic percentages taken from 6 different points are at. 7.78%, 80.69% and 11.52%, which are in good aggrement with the expected values (La 7%, Fe 83%, %10 Si).

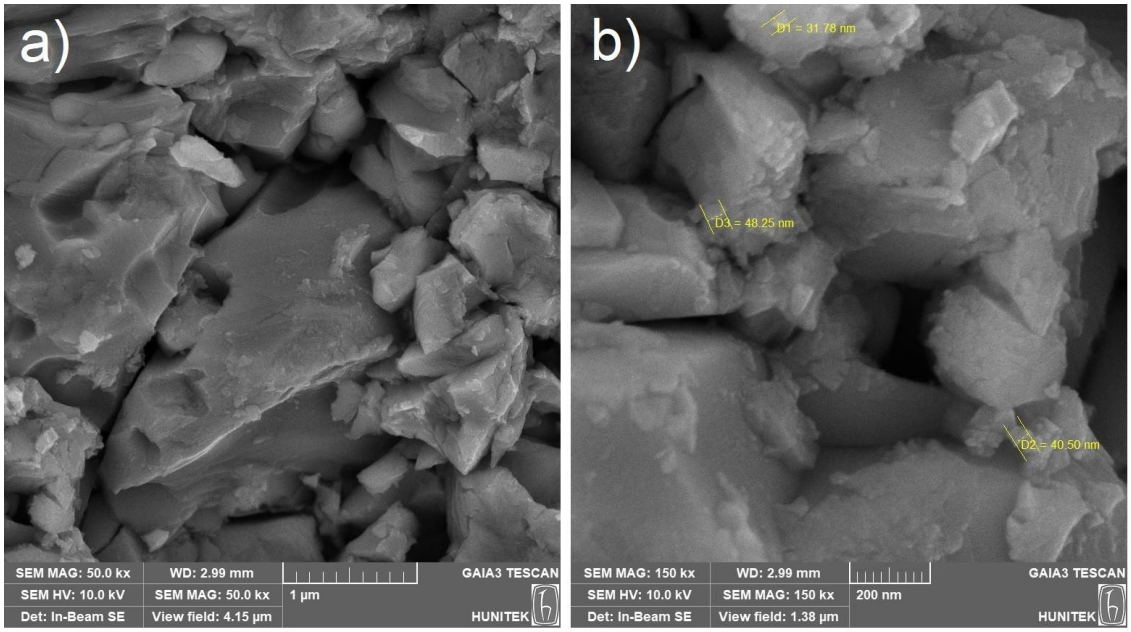

Figure 4.3. SEM images of the parent compound.

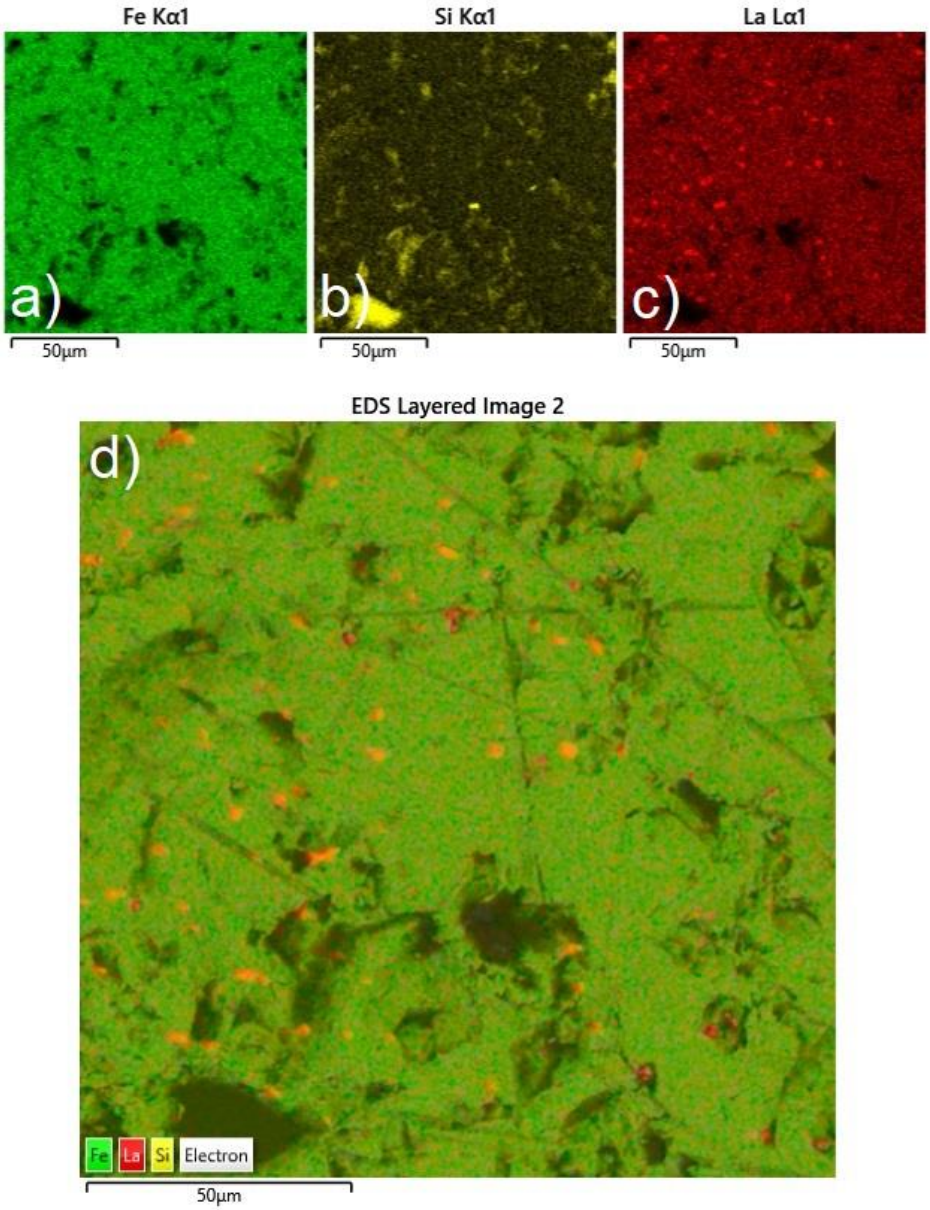

Figure 4.4. EDS mapping images of the parent compound

4.3. Magnetic Properties of Bulk LaFeSi

The room temperature hysterisis curves of the bulk samples are shown in Figure 4.5. The samples annealed for 4 and 7 days are ferromagnetic whereas 10 day shows paramagnetic behavior. The cubic $La(FeSi)_{13}$ is paramagnetic at room temperature with Curie point well below 300 K. Ferromagnetic signal observed for samples annealed for 4 and 7 day are due to the existance of iron impurity, as shown in XRD patterns (Figure 4.2.).

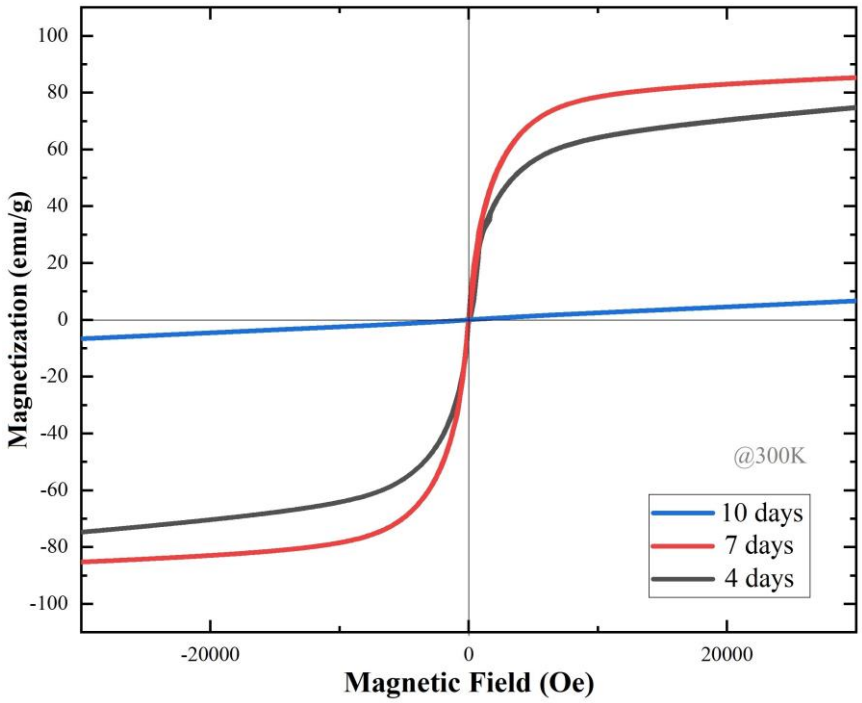

Figure 4.5. Hysterisis curves of LaFeSi compounds, at room temperature.

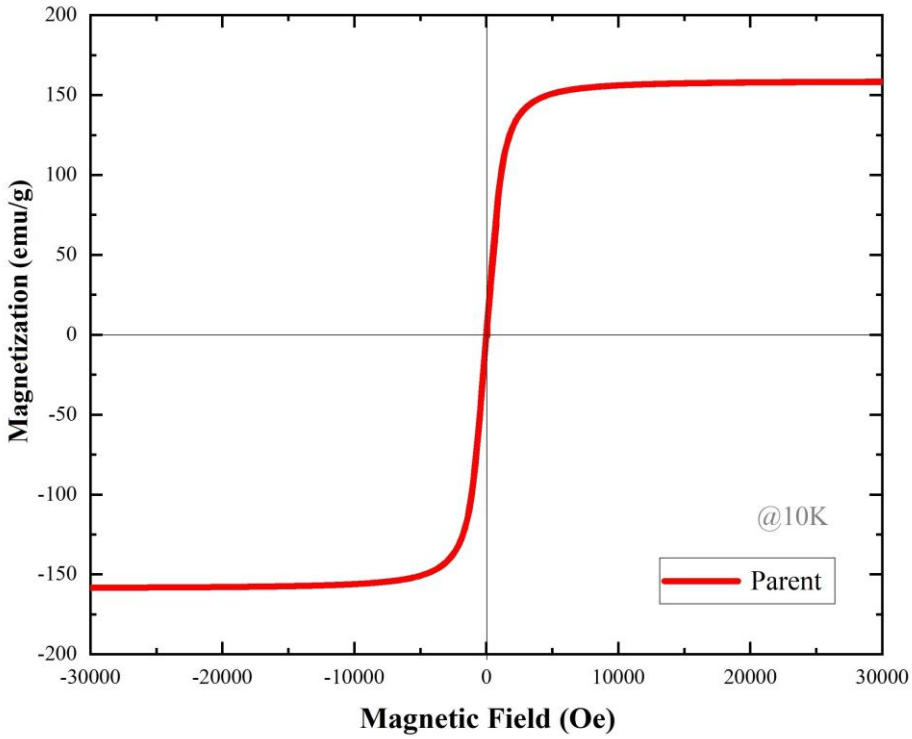

Figure 4.6. M-H curve of parent LaFeSi compound at 10 K.

As depicted in Figure 4.6, the parent LaFeSi compound is in ferromagnetic state at 10 K. The saturation magnetization value at 10 K, for $LaFe_{11.57}Si_{1.43}$ (158 emu/g) is in good aggrement with the value reported in literature, which is 181.0 emu/g measured at 2 K for $LaFe_{11.4}Si_{1.6}$ [32].

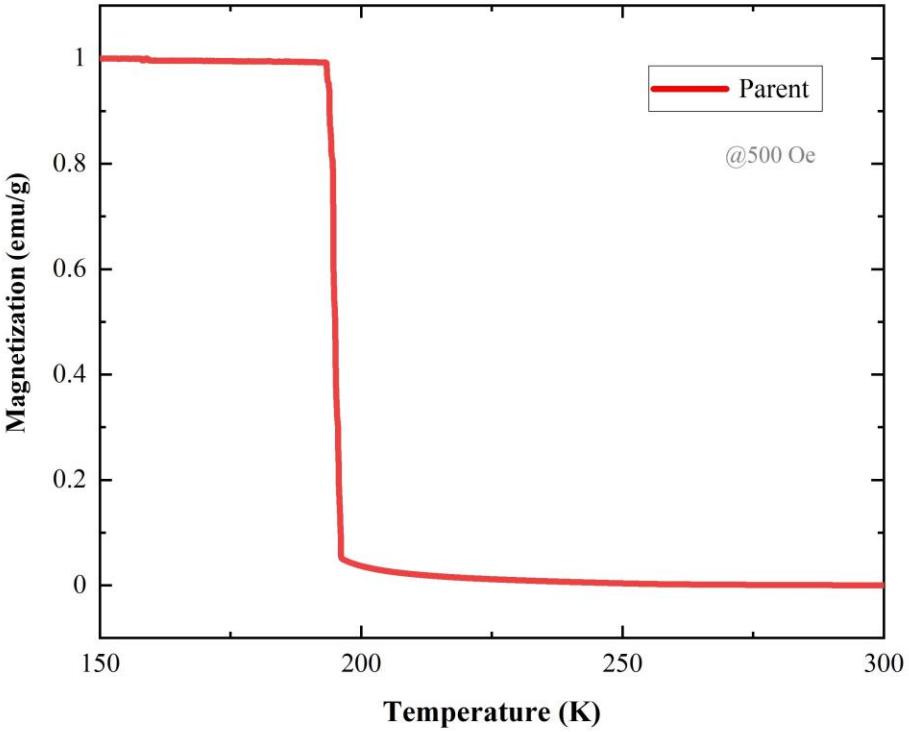

Figure 4.7. M-T curve of parent LaFeSi compound in the presence of 500 Oe applied field.

Figure 4.7. shows the M-T curve of the parent compound. The sharp change of the magnetization at 195 K is the Curie point of the sample. This Curie temperature where the first order magnetic phase transition occured is found to be consistent with the previously reported values [40].

5. HYDROGENATION OF LAFESI

5.1. Hydrogenation of LaFeSi using Sievert Apparatus

Here, hydrogenation process of the $LaFe_{11.57}Si_{1.43}$ samples was made in two steps, firstly hydrogen insertion using Sieverts' apparatus, secondly hydrogen level adjusting via vacuum-heating.

5.1.1. Hydrogen Insertion in LaFeSi by Thermal Treatment

In this step, homogenized compounds are crushed and powdered, as shown in Figure 5.1. The powder samples are hydrogenated by thermal diffusion. In this method, samples are loaded to Sievert-type apparatus after being weighed at precision scale. Samples were hydrogenated at 5 bar H_2 atmosphere and 200 °C for 60 and 30 minutes, and 2 bar H_2 atmosphere and 200 °C for 30 minutes (Table 5.1). The change in the hydrogen gas pressure is measured using Sievert. Hydrogen diffusion amount of the samples are calculated by using the difference in the sample mass between pre-process and post-process, the amount of change in the H_2 gas pressure and the volume of the room that sample is loaded in by using the Ideal Gas Equation given in Eq.2.

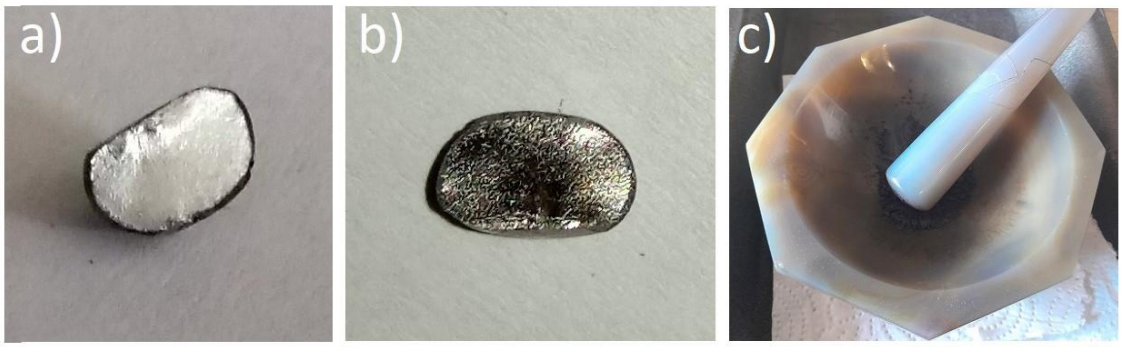

Figure 5.1. a-b) Crushed LaFeSi samples, c) powdering step.

Table 5.1. Synthesis parameters of hydrogenated LaFeSi samples via Sievert-type apparatus, along with their abbreviated names. ("PS-…b-…m": **P**arent sample hydrogenated with **S**ievert apparatus under …**b**ar H_2 for …**m**inutes)

Sample Name	H_2 gas pressure (bar)	Duration (min)

PS-2b-30m	2	30
PS-5b-30m	5	30
PS-5b-60m	5	60

5.1.2. Adjusting Hydrogenation Level of LaFeSi Powders

To adjust the hydrogenation amount for controlling the Curie Temperature, hydrogen saturated samples by Sievert were then annealed at 150 - 280 °C under vacuum of 0.1 mbar for 5 minutes, with a heating rate of 8 °C/min by using a Lindberg Blue M tube furnace (Figure 3.4-b). Abbreviated sample names are summarized in Table 5.2. for ease of reading.

Table 5.2. Synthesis parameters of H content adjusted LaFeSiH samples by vacuum heating, along with their abbreviated names. ("PSV-...d": **P**arent sample hydrogenated with **S**ievert apparatus and **V**acuum annealed at ...Celcius **d**egree for 5 minutes, "PSV-...d-60m": **P**arent sample hydrogenated with **S**ievert apparatus and **V**acuum annealed at ...celcius **d**egree for **60 m**inutes)

Sample Name	Temperature (°C)
PSV-150d	150
PSV-200d	200
PSV-220d	220
PSV-250d	250
PSV-265d	265
PSV-280d	280
PSV-280d-60m	280

5.1.3. Structural Measurements of LaFeSi powders Hydrogenated by Sievert Apparatus

5.1.3.1. XRD Analysis

Intersititial hydrogen insertion into the compound causes the expansion in the structure, which causes a significant peak shifts in XRD patterns around 0.40° - 0.68° degrees, as shown in Figure 5.2 and Table 5.3. In Figure 5.2 oxide phases and α-Fe impurities were seen in PS-5b-30m and PS-2b-30m samples. In the hydrogenation process that took place for 60 minutes with 5 bar H_2 gas pressure, high purity sample is obtained. Morever, the peak widths is increased after hydrogenation process. This result can be explained by intra-intergranular cracks due to the hydrogen embrittlements in the crystal structure of the material.

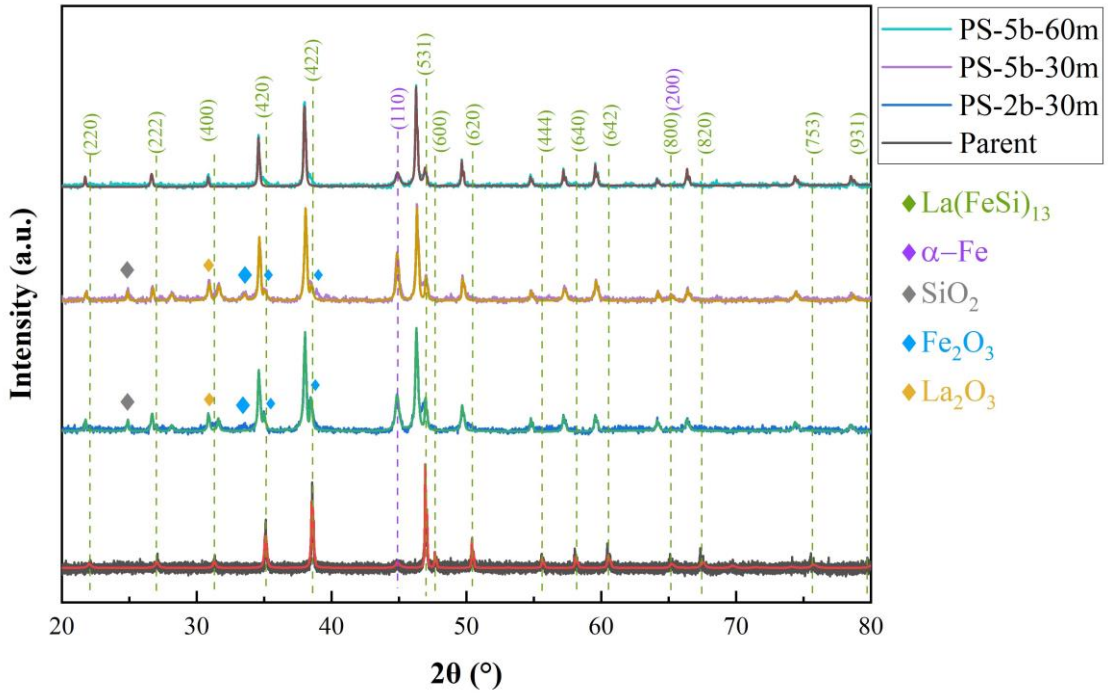

Figure 5.2. XRD patterns of hydrogenated LaFeSi compounds via Sievert apparatus.

Table 5.3. XRD results of hydrogenated LaFeSi parent compound via Sievert-type apparatus. ("PS-…b-…m": **P**arent sample hydrogenated with **S**ievert apparatus under …**b**ar H_2 for …**m**inutes)

	LaFeSiH phase fraction (wt%)	Lattice parameter (Å)	Lattice Expansion (%)	Oxide phase fraction (wt%)	Iron phase fraction (wt%)
PS-2b-30m	73.2±0.7	11.5801±0.0002	1.15	10.5±0.4	16.3±0.3
PS-5b-30m	80.1±0.5	11.5952±0.0004	1.28	3.8±0.3	16.1±0.3
PS-5b-60m	91.2±0.6	11.6211±0.0007	1.51	-	8.8±0.4
Parent Sample	94.4±0.4	11.4483±0.0005	-	-	5.6±0.4

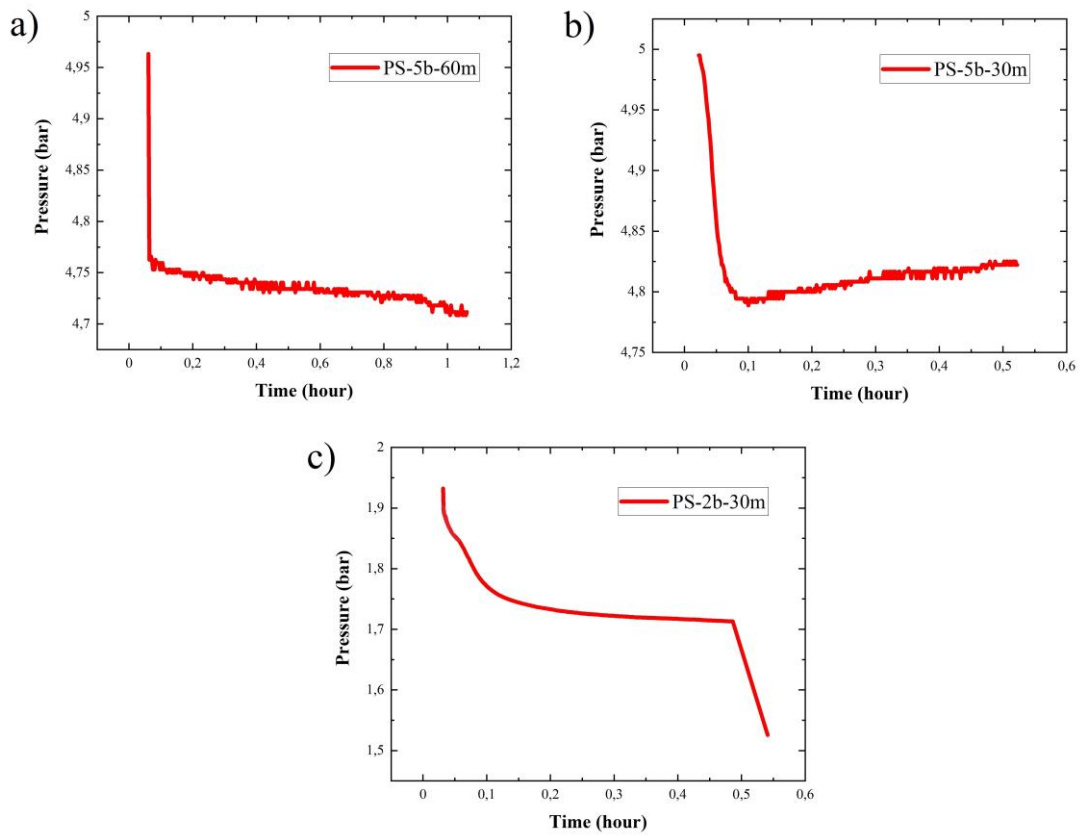

Figure 5.3. The amount of hydrogen pressure change during hydrogenation process of a) PS-5b-60m, b) PS-5b-30m, c) PS-2b-30m, by using Sievert.

The hydrogen content "y" of the samples $La(FeSi)_{13}H_y$ are calculated by using Ideal Gas Equation (Eq.2.). Results are summarized in Table 5.4. All the samples are almost saturated to H with y values of 2.22 to 2.32, which is in accordance with the previous reports [60].

Table 5.4. Calculated H contents in $La(FeSi)_{13}H_y$

	y value	Vial volume (10^{-6} cm^3)	H_2 gas pressure change (bar)	Sample mass (g)
PS-2b-30m	2.22	11.37	0.1157	0.3469
PS-5b-30m	2.22	11.38	0.1237	0.3730
PS-5b-60m	2.32	9.51	0.2642	0.6360

The XRD patterns in Figure 5.4 reveal changes in the samples' structure after vacuum heating process aimed at adjusting the hydrogen amount. An increase in the α-Fe impurity phase is evident [61]. Notably, the sample vacuum-heated at a higher temperature (PSV-280-60m, Table 5.5 exhibits a more substantial rise in the α-Fe phase. No oxide phases are detected. The broadening of peak widths after the vacuum-heating process is attributed to the insertion/deinsertion of hydrogen atoms into the material's structure, inducing stress and strain. This phenomenon leads to embrittlement and crack propagation in the crystal structure, consequently broadining the XRD peaks [62],[63]. A significant reduction in lattice expansion percentage and XRD peak shift in the PSV-280d-60m sample after vacuum heating suggests a high level of hydrogen deinsertion.

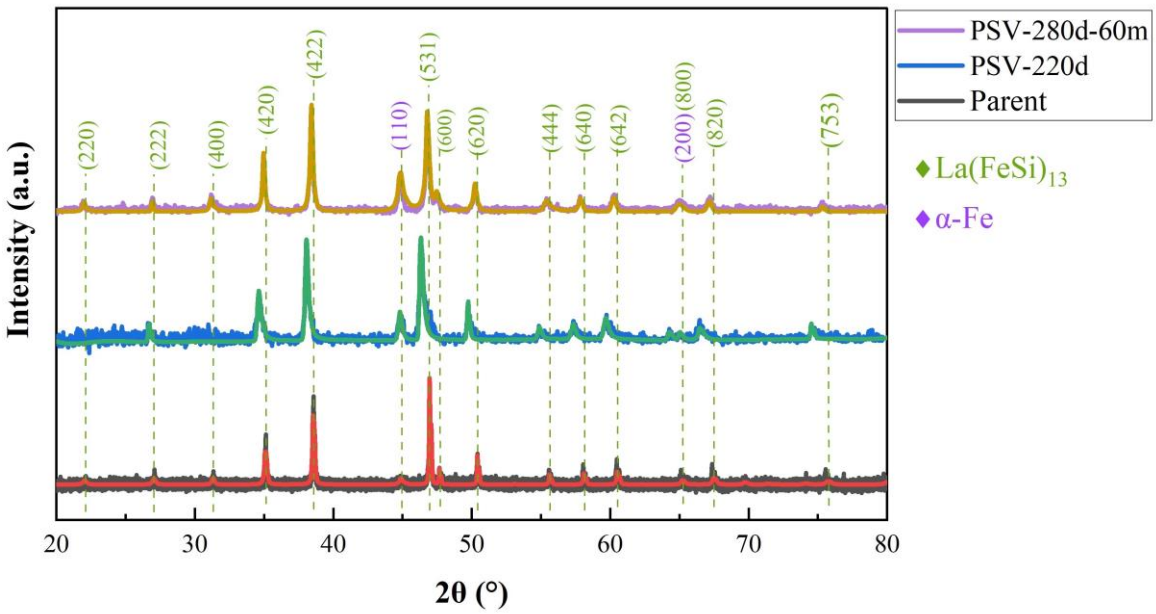

Figure 5.4. XRD patterns of PSV-220d, PSV-280d-60m and parent sample.

Table 5.5. Calculated parameters from Rietveld refinements of hydrogen content adjusted LaFeSiH samples.

	LaFeSiH phase fraction (wt%)	Lattice parameters (Å)	Crystal structure	Lattice expansion (%)	Fe phase fraction (wt%)
PSV-220d	91.65±0.02	11.5802±0.0004	Cubic	1.18	8.35±0.03

PSV-280d-60m	89.29±0.05	11.5001±0.0007	Cubic	0.45	10.71±0.05

The hydrogenation amount of the samples after vacuum annealing is determined by the complete hydrogen removal from the samples via Sievert. For that purpose samples are heated at 200 °C and the change in the pressure with time is measured, as shown in Figure 5.5. The y value is calculated as 1.41, confirming the successful control of H content in the sample.

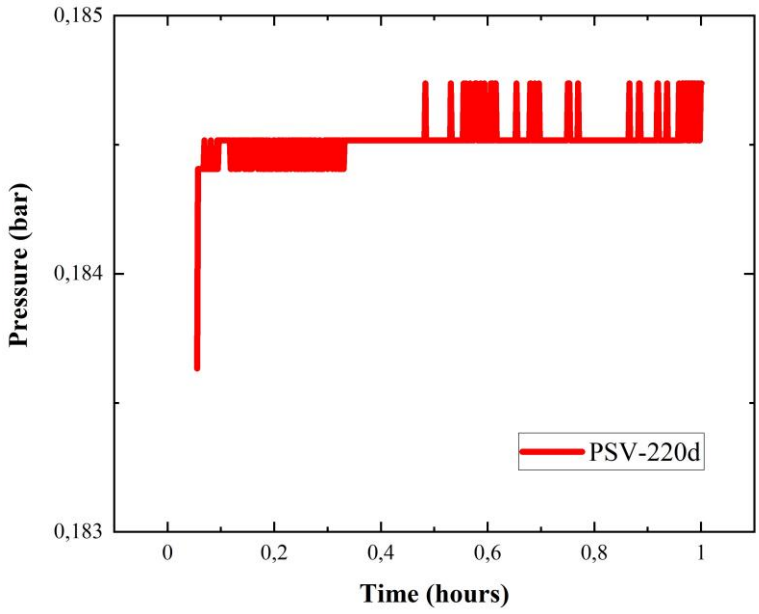

Figure 5.5. Hydrogen gas pressure change over time in PSV-220d sample.

5.1.3.2. SEM and EDS Analysis

Figure 5.6 shows SEM micrographs of PS-5b-60m, PS-5b-30m and PS-2b-30m samples. There are no cracks observed in the powdered parent sample shown in Figure 4.3-a. However, in Figure 5.6-a, b and c, cracks are observed. Thermally or hydrogen induced expansions cause defects and stresses in the structure, which result in cracks [64],[65]. Since the sample was powdered by hand-crushing by using pestle and mortar, particle sizes are big and size distribution is also wide. The EDS spectras for PS-5b-60m sample

are shown in Figure 5.7. Measurements are taken from four different points and average elemental compositions are summarized in Table 5.6.

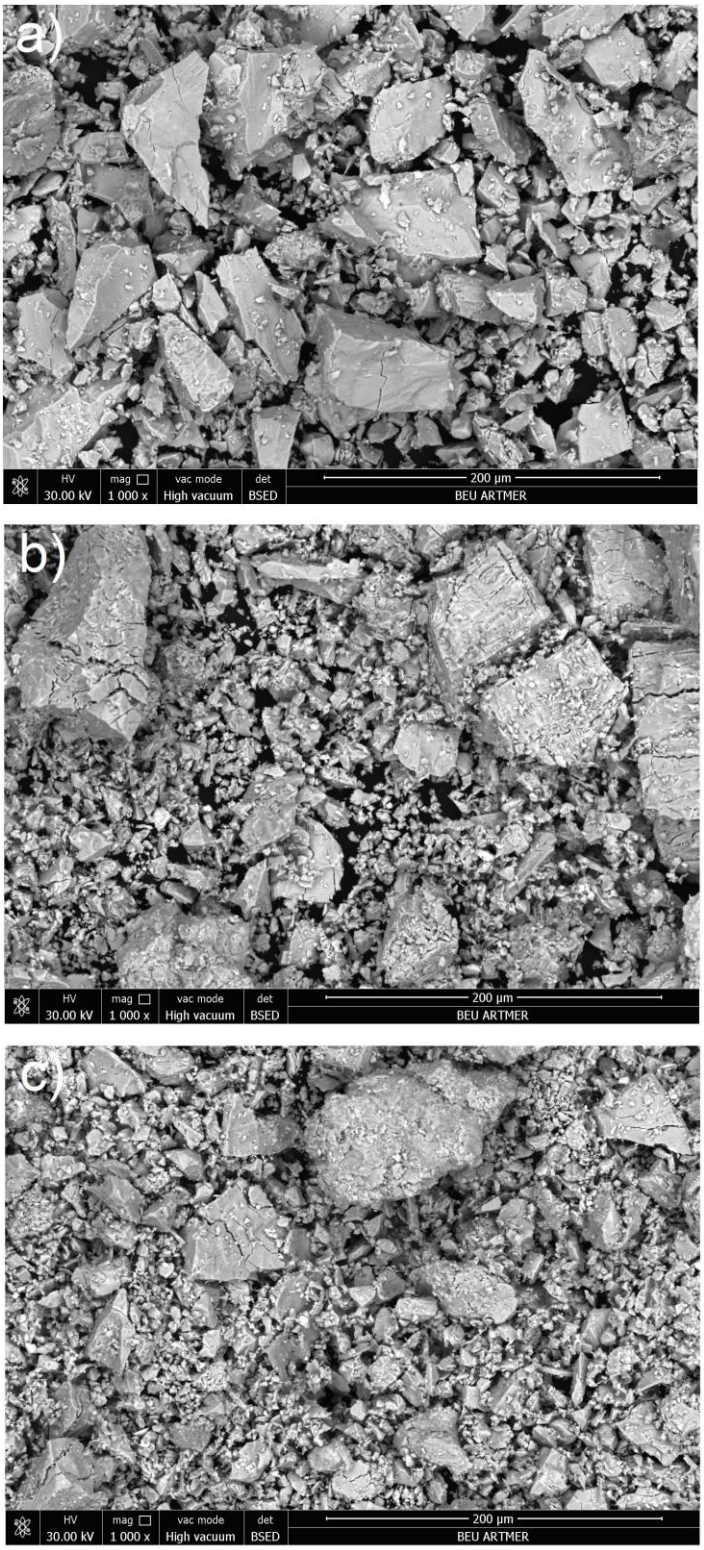

Figure 5.6. SEM images of a) PS-5b-60m, b) PS-5b-30m and c) PS-2b-30m samples with

200 µm scale.

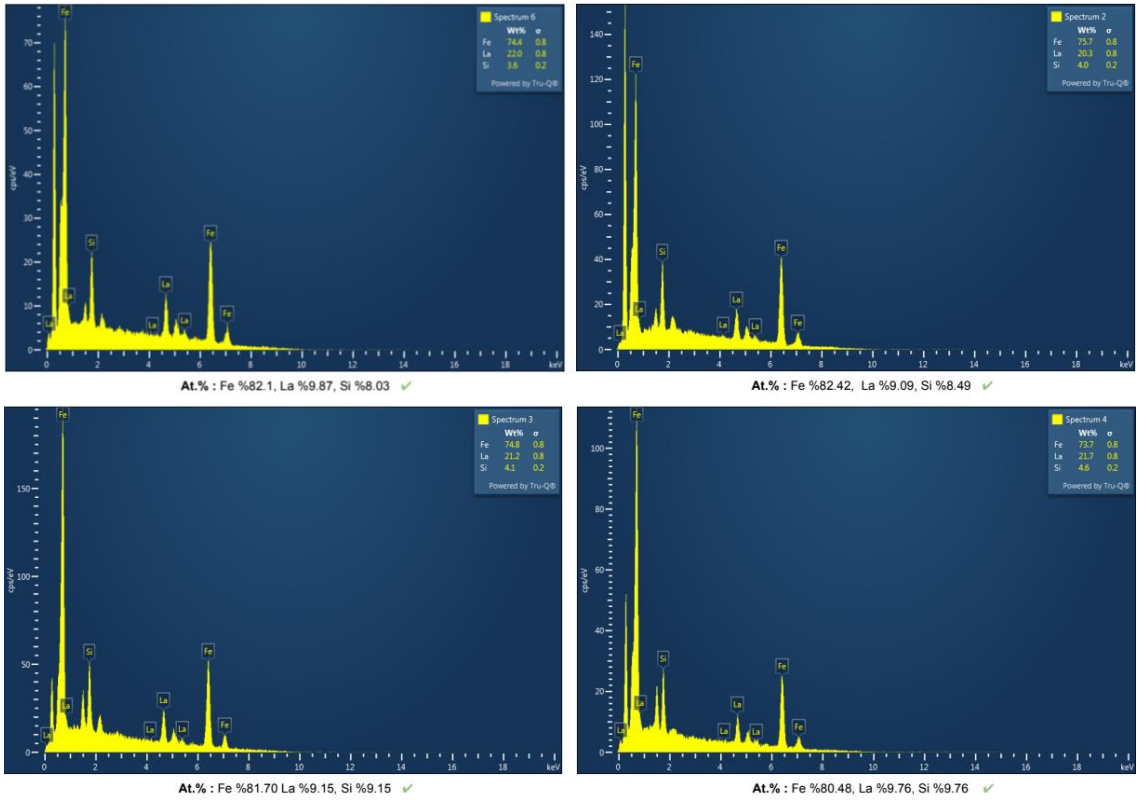

Figure 5.7. EDS spectra of PS-5b-60m sample.

Table 5.6. Average atomic compositions for PS-5b-60m sample.

	Average Measured at.%	Expected at.%
Fe	81.68	83
La	9.47	7
Si	8.86	10

Figure 5.8 shows SEM images of PSV-220d sample. During hydrogen insertion and deinsertion, hydrogen atoms may interact with dislocations and may promote transgranular and grain boundary cracks [62],[63], as seen in Figure 5.8-b.

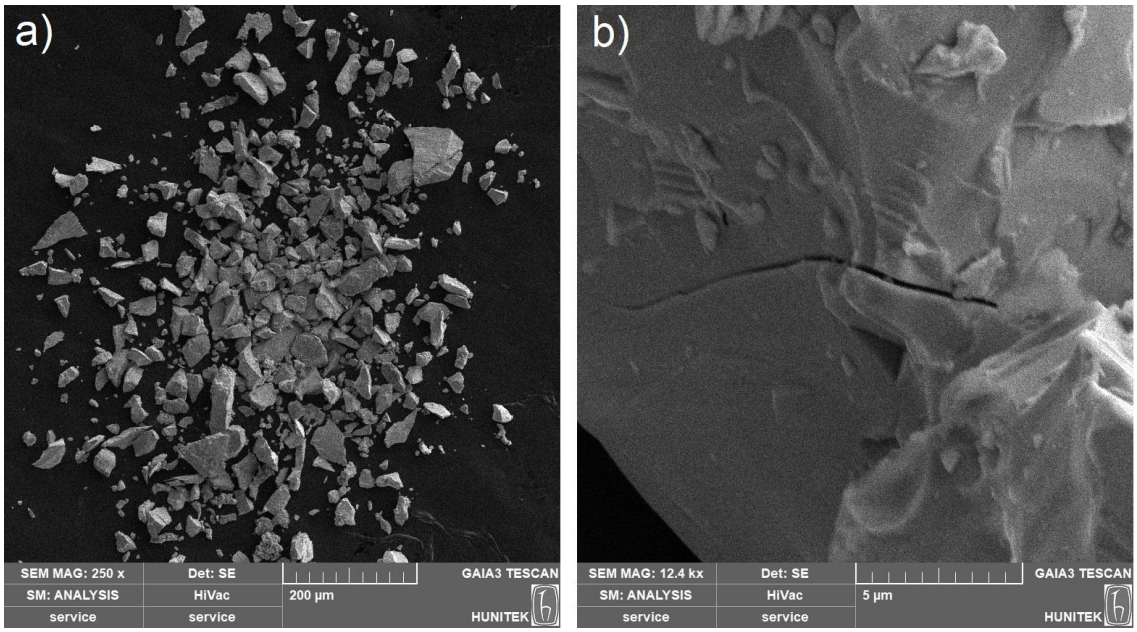

Figure 5.8. SEM images of PSV-220d sample

5.1.4. Magnetic Measurements of LaFeSi powders Hydrogenated by Sievert Apparatus

Figure 5.9 illustrates that PS-5b-60 ($La(FeSi)_{13}H_{2.32}$) exhibits ferromagnetic behavior at room temperature. This is in contrast to the paramagnetic behavior observed in the parent sample, as depicted in Figure 4.5. The successful shift of the Curie point above room temperature after hydrogenation is evident. The magnetic saturation value of 127 emu/g at 300 K for $La(FeSi)_{13}H_{2.32}$ aligns closely with the literature value, approximately 130 emu/g [40]. This finding indicates that the hydrogenation process has effectively induced ferromagnetism in the material, and the measured magnetic saturation value is consistent with previously reported values in the literature.[40].

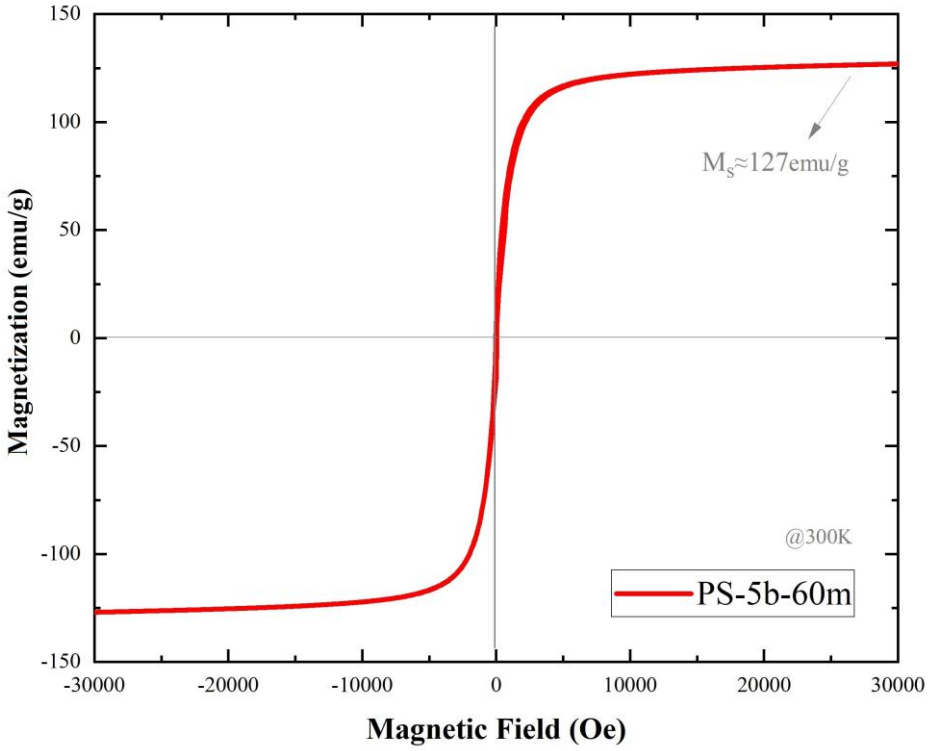

Figure 5.9. Room temperature hysterisis curve of PS-5b-60m hydrogenated LaFeSi compound via Sievert.

In Figure 5.10, it is evident that the Curie temperature (T_C) shifts to around 350 K for the hydrogenated samples. This notable change in the T_C value after hydrogenation can be attributed to the magneto-volume effect. The lattice expansion induced by hydrogenation plays a key role in this effect, and it is associated with a characteristic feature observed in the itinerant-electron metamagnetic effect. The magneto-volume effect, influenced by alterations in the crystal lattice due to hydrogen insertion, contributes to the observed shift in the Curie temperature. This result underscores the sensitivity of the magnetic properties to structural changes induced by hydrogenation in the $La(FeSi)_{13}H_{2.32}$ samples, emphasizing the intricate interplay between structural and magnetic characteristics in the material. [66]. In Figure 5.10, it is observed that the 1st-order magnetic phase transition becomes slower after the hydrogenation step. This deceleration in the transition may be attributed to size reductions resulting from stress-induced fractures during the hydrogenation process or the instability of the compound due to hydrogen redistributions

within the material [59],[61],[65]. The persistence of magnetization values following the phase transition could be influenced by the presence of a ferromagnetic α-Fe impurity phase, which has much higher Curie point (1043 K). Additionally, oxides such as Fe2O3, also with a higher Curie point of 948 K, might contribute to the sustained magnetization values [67]. These findings suggest that the hydrogenation process not only alters the kinetics of the magnetic phase transition but also introduces complexities related to material stability and impurity phases, contributing to the observed changes in the magnetic behavior.

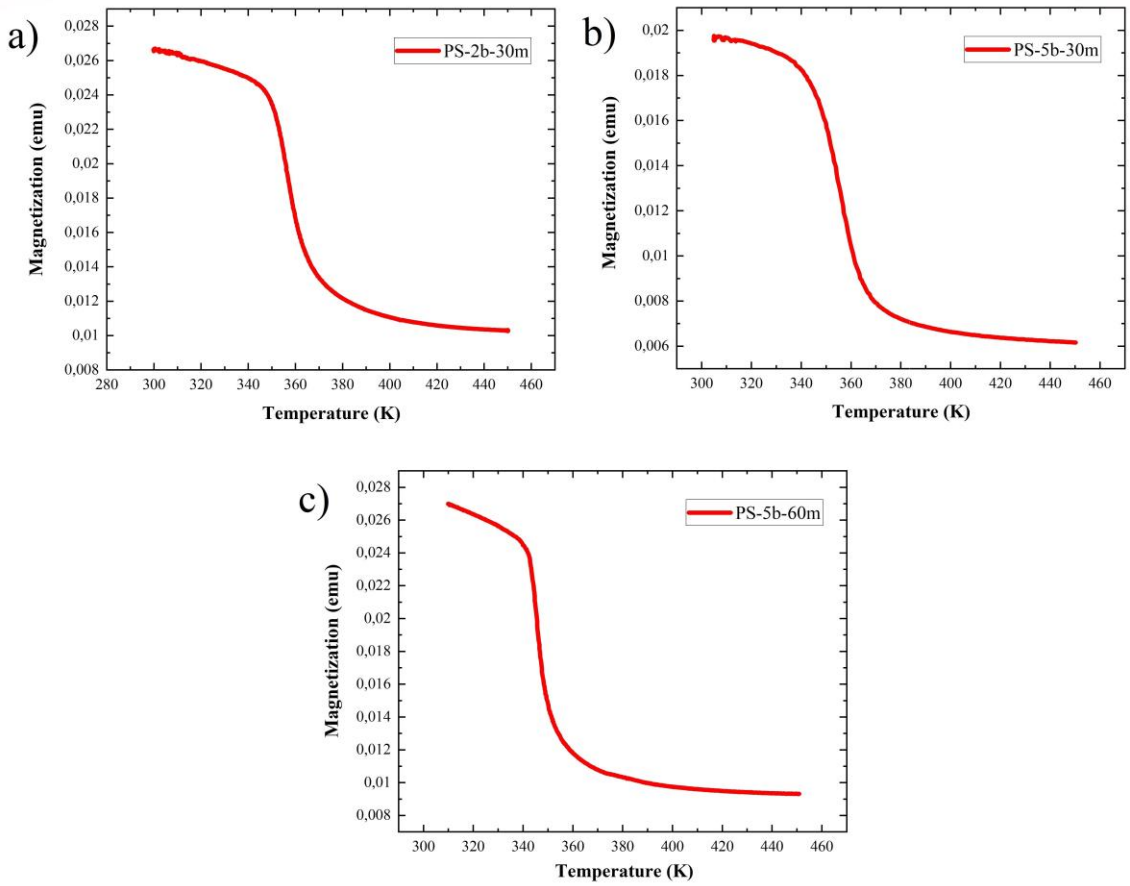

Figure 5.10. M-T curves of hydrogenated a) PS-2b-30m, b) PS-5b-30m, c) PS-5b-60m samples via Sievert, in the presence of 500 Oe applied field.

Figure 5.11 illustrates the variation of the Curie point with the vacuum heating temperature. The data demonstrates the successful adjustment of the Curie temperature

within the range of 240 K and 350 K. This controlled tuning of the Curie temperature is a significant achievement, allowing for tailored magnetic properties in the LaFeSiH samples. The achievement of T_C value around 50 °C, suitable for effective use in magnetic hyperthermia applications as monotherapy, is demonstrated in the PSV-220d sample with a T_C value of 319 K (46 °C) [13]. The T_C values for samples vacuum-annealed at different temperatures for 5 minutes are presented graphically in Figure 5.12.

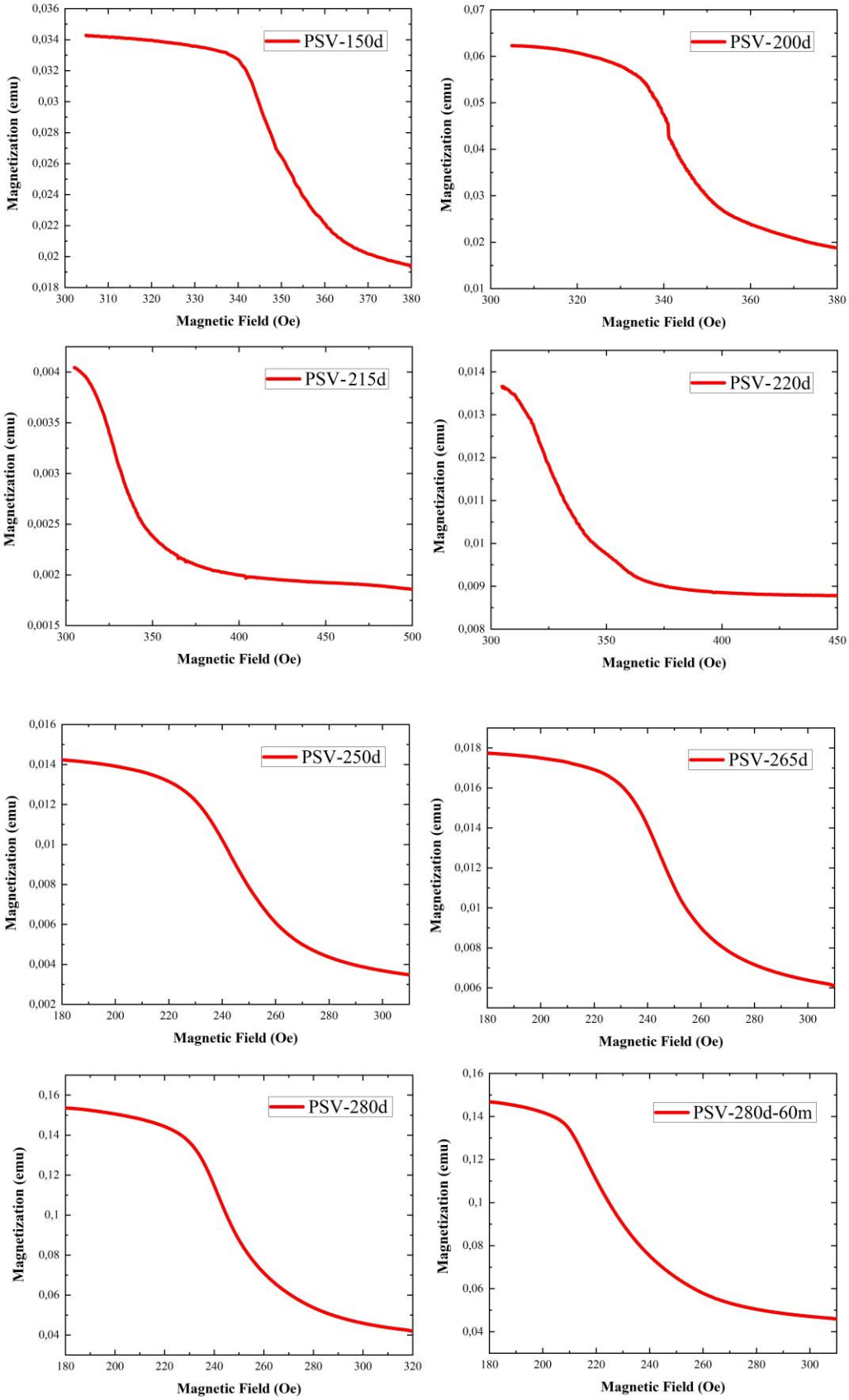

Figure 5.11. M-T plots of vacuum annealed LaFeSiH samples in the presence of 500 Oe applied field.

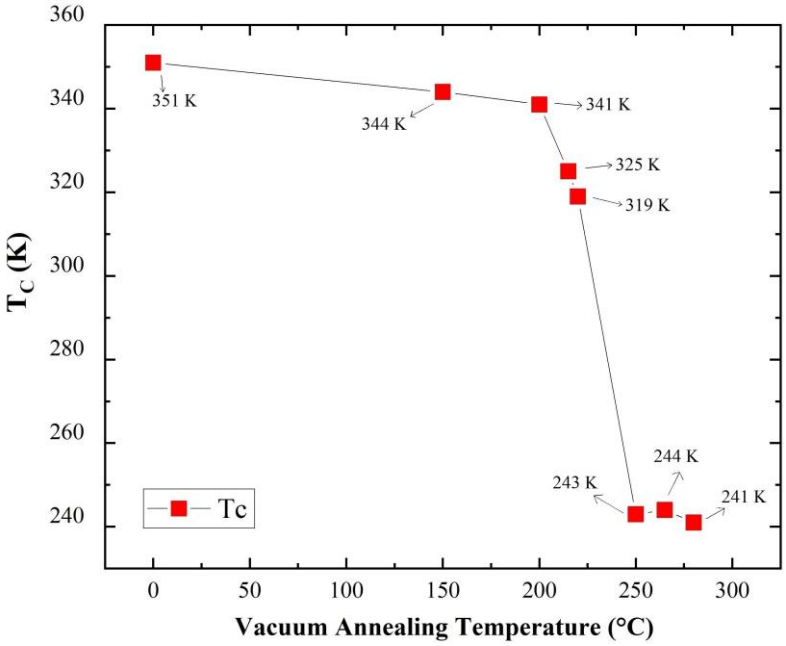

Figure 5.12. Curie Temperature of samples hydrogenated by different vacuum annealing temperature using Sievert.

To produce LaFeSiH nanopowders, the samples are milled at a speed of 400 rpm in a 50 mL zirconium oxide grinding jar. Figure 5.13. displays the M-T plot of the parent sample after being hydrogenated for 60 minutes under 5 bar H_2 gas following 30 minutes of milling. The results reveal that, despite a deceleration in the first-order phase transition, the sharpness of the transition is maintained.

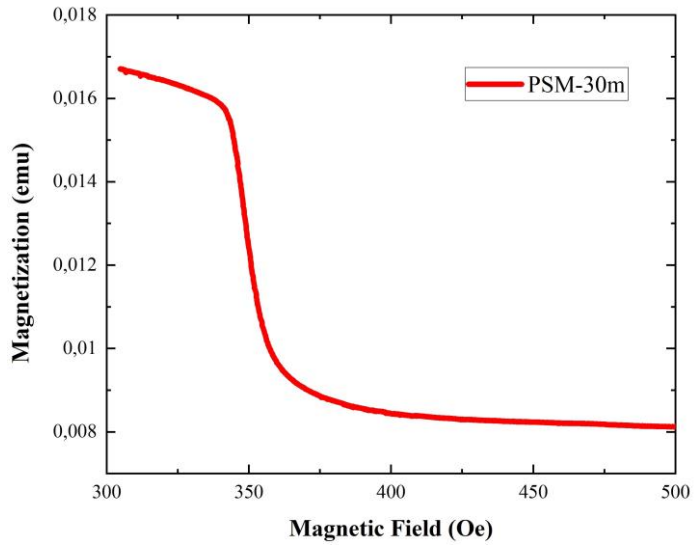

Figure 5.13. M-T curve of PS-5b-60m $(La(FeSi)_{13}H_{2.32})$ sample milled for 30 min.

5.1.5. Magneto-Thermal Properties of LaFeSi powders Hydrogenated by Sievert

Figure 5.14 shows the heating performance of PSV-220d sample with Curie point at 46 °C. The temperature rise stopped around 54 °C which can be caused by the remaining α-Fe phases continuing their heating. Benz et al. also reported that α-Fe precipitation has a significant effect on magneto-themal measuremets [41]. SAR value for PSV-220d is calculated as 10.9±0.2 W/g. The observation that the ferrofluid temperature reached 50 °C in less than 7 minutes indicates a rapid and efficient heating performance of the system.

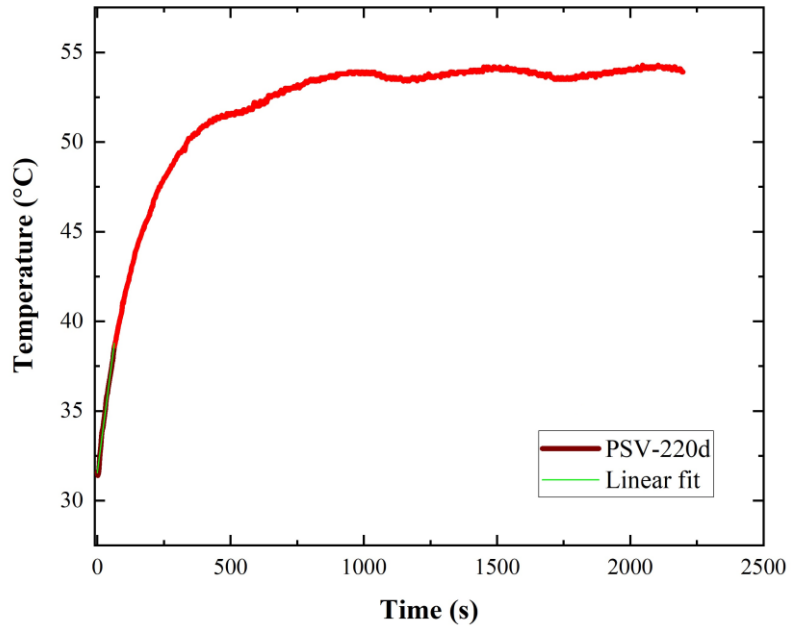

Figure 5.14. Temperature vs. time plot of PSV-220d sample under AMF.

Figure 5.15 depicts the heating performance of the PS-5b-60m sample, which was milled for 30 minutes, with a concentration of 20 mg magnetic powder per 2 mL ethanol. The particle size reduction achieved through the milling process contributes to better suspension of particles in the fluid volume, resulting in a more homogenized heating performance.

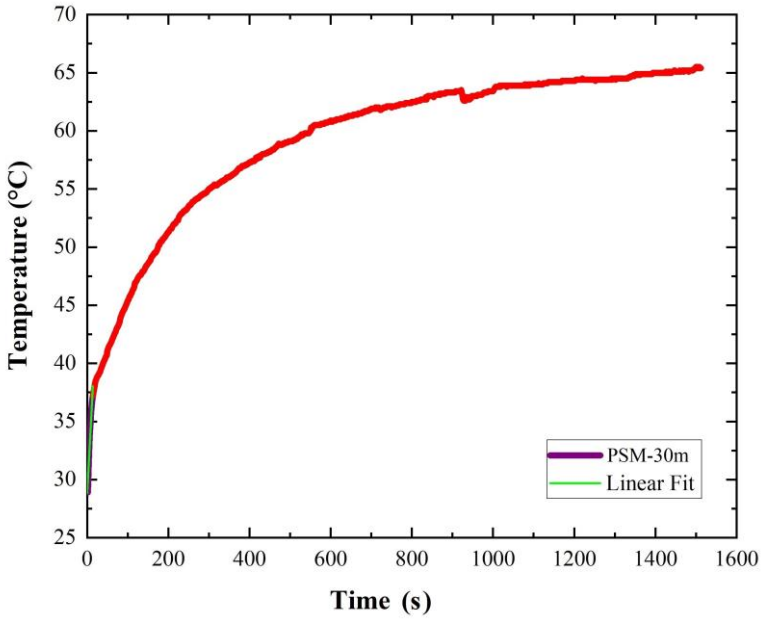

Figure 5.15. Temperature vs. time plots of PS-5b-60m sample milled for 30 min.

Table 5.7. SAR values calculated for PS-5b-60m and 30 min. milled samples. ("PSM-30m": PS-5b-60m sample milled for 30 min)

	SAR (W/g)
PS-5b-60m	69 ±8
PSM-30m	127 ±12

5.2. Hydrogenation of LaFeSi using Ball-Milling

In the second method for hydrogenating the samples, the powdered samples are milled in the presence of H_2 gas under 5 bar pressure. This milling process take place in a 250 mL steel vial with a 1:40 powder-to-ball ratio, and a milling speed of 400 rpm, utilizing the Retsch PM 100 ball miller (Figure 3.6). The samples underwent milling for durations ranging from 10 to 300 minutes. To conduct this process, the samples are initially loaded into a steel jar, and the vial is securely locked within a glove-box. The jar was then purged three times with 1 bar H_2 gas through the valve on the jar lid. The pressure inside the vial is monitored using the PressurePro monitoring system and a pressure sensor mounted on one of the valves on the jar lid. Figure 5.16 illustrates the pressure reading system and the

jar with the pressure sensor. The samples produced in this phase of the study are listed in Table 5.8 with abbreviated sample names.

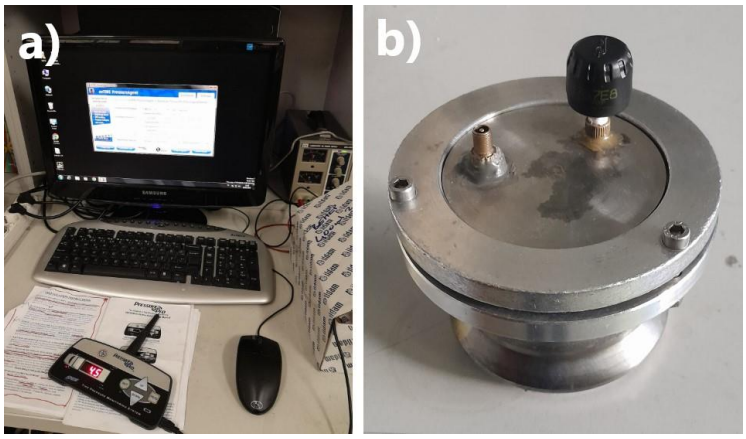

Figure 5.16. a) Pressure reading system, b) locked jar with pressure sensor.

Table 5.8. Synthesis parameters of hydrogenated LaFeSi samples via ball-mill, with abbreveated sample names. (“PM-...m” : **P**arent sample **M**illed for ...**m**inutes)

Sample Name	Milling time (min)
PM-30m	30
PM-60m	60
PM-180m	180
PM-300m	300

5.2.1. Structural Measurements of LaFeSi powders Hydrogenated by Ball-Milling

5.2.1.1. XRD Analysis

The X-ray diffraction patterns of the hydrogenated samples via ball-milling are presented in Figure 5.17, and the Rietveld refinement results are provided in Table 5.9. Oxide phases are observed in the XRD patterns of PM-30m and PM-60m samples. The increase in peak intensity at 45° with the increasing milling time indicates a rise in the α-Fe phase with prolonged milling time. This could be attributed to the instability of the partially hydrogenated LaFeSi compounds [61]. Additionally, interactions between steel balls during milling may introduce some α-Fe impurity into the samples, proportionate to the

milling time. As a manifestation of lattice expansion due to hydrogen insertion, shifts to the left side in peaks of the LaFeSi phase are observed. The decreasing sharpness of the peaks with increasing milling time suggests a reduction in crystallinity. The crystallite size is found to decrease with increasing milling time, as indicated in Table 5.9, which aligns with expectations for a milling process. However, in the sample milled for 300 minutes, the crystallite size starts to increase again. This phenomenon may be attributed to particles coalescing due to excessive energy input [68]. These observations highlight the intricate structural changes occurring during the ball-milling hydrogenation process.

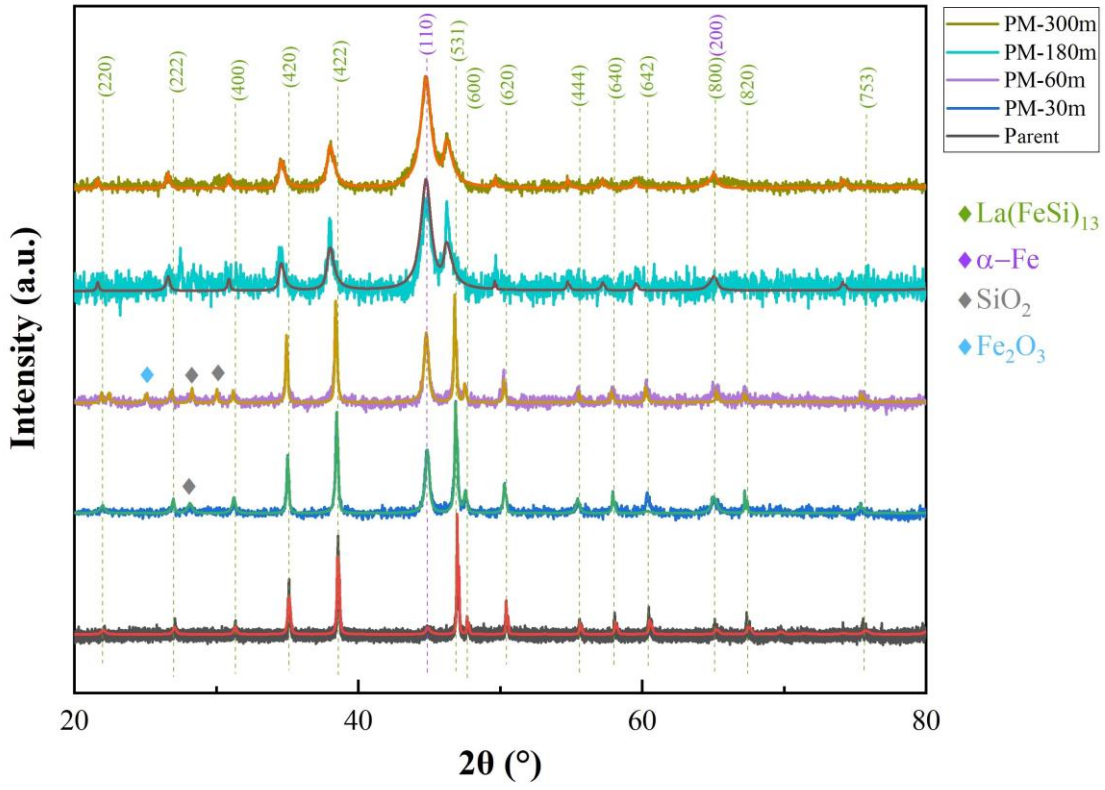

Figure 5.17. XRD patterns of hydrgenated LaFeSi compounds via ball-milling.

Table 5.9. XRD results of hydrogenated LaFeSi compounds via ball milling.

	LaFeSiH phase fraction (wt%)	Lattice parameter (Å)	Lattice Expansion (%)	Iron phase fraction (wt%)	Crystallite size (nm)

PM-30m	74.4±0.4	11.4832±0.0003	0.18	25.6±0.3	31.7
PM-60m	68.8±0.5	11.4834±0.0006	0.35	31.2±0.5	27.4
PM-180m	47.6±0.2	11.6090±0.0006	1.40	52.4±0.5	11.8
PM-300m	29.6±0.9	11.6370±0.0006	2.10	70.4±0.9	17.3

5.2.1.2. SEM and EDS Analysis

Figure 5.18 shows the SEM images of parent and milled samples, in comparison. Magnetic particles tend to agglomerate, due to the magnetic dipole-dipole interactions [69]. While hydrogenating LaFeSi samples under 5 bar H_2 atmosphere with ball-milling, reduction in particle size is also observed due to the mechanical impact.

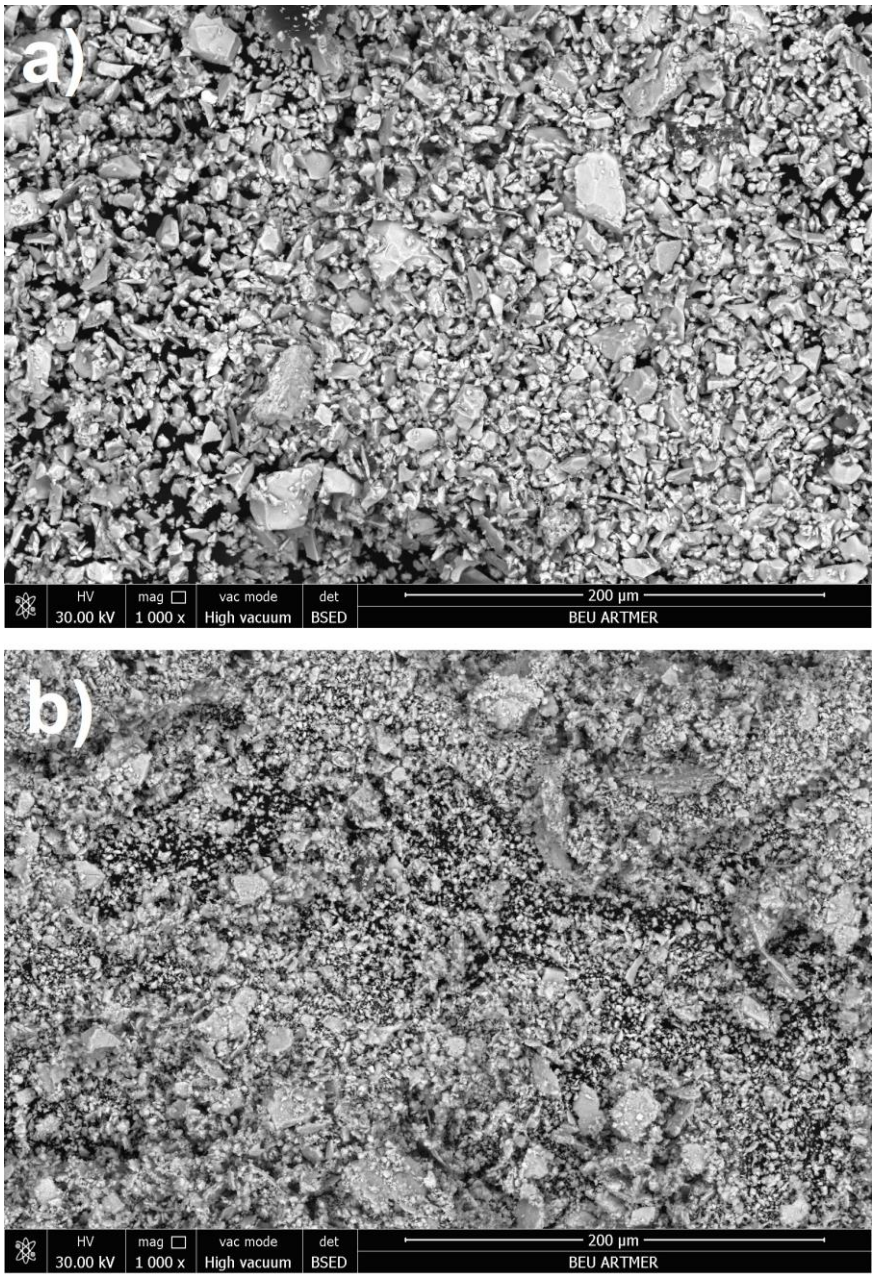

Figure 5.18. SEM images of a) parent LaFeSi sample b) PM-300m.

5.2.2. Magnetic Measurements of LaFeSi powders Hydrogenated by Ball-Milling

Room temperature hysterisis curves of hydrogenated LaFeSi compounds using ball-milling are given in Figure 5.19. The samples ahow ferromagnetic behavior due to the dominant α-Fe phase [61]. Morever, the Curie transition cannot be observed around room temperature as seen in Figure 5.20 due to deterioration of the fcc-LaFeSi structure and big size-distribution.

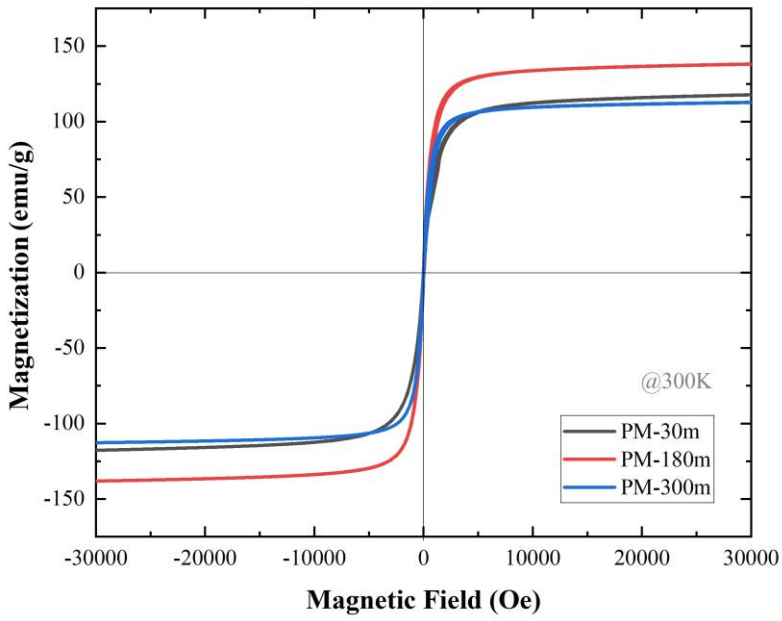

Figure 5.19. M-H curve of hydrogenated LaFeSi compounds by ball-milling, at room temperature.

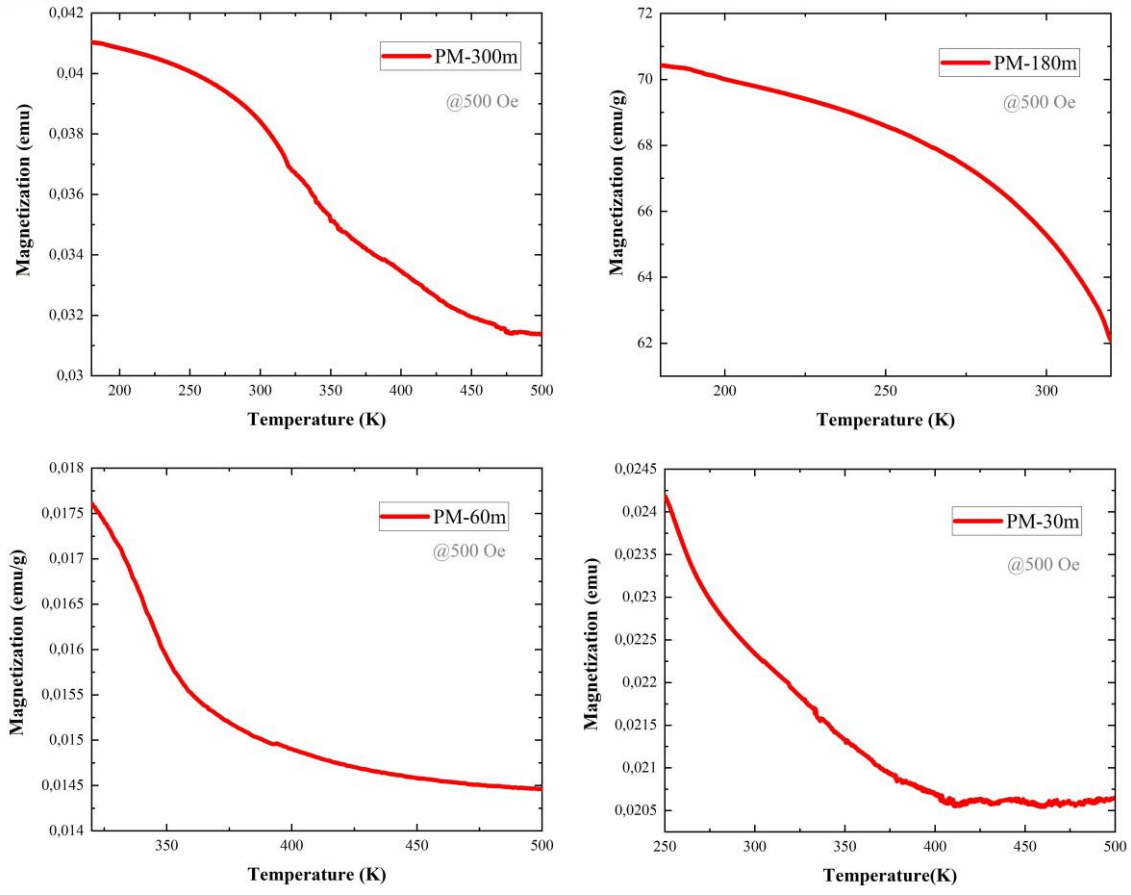

Figure 5.20. M-T curves of LaFeSi samples hydrogenated by ball-milling.

5.2.3. Magneto-Thermal Measurements of LaFeSi powders Hydrogenated by Ball-Milling

Figure 5.21 illustrates the heating performance of hydrogenated LaFeSi samples using a ball mill, and Table 5.10 provides a summary of the SAR values. The results indicate that SAR values increase with longer milling times, attributed to the rising α-Fe content. Moreover, particles with reduced sizes, achieved through milling, have the capability to disperse more homogeneously in the liquid, leading to enhanced heating of the volume.

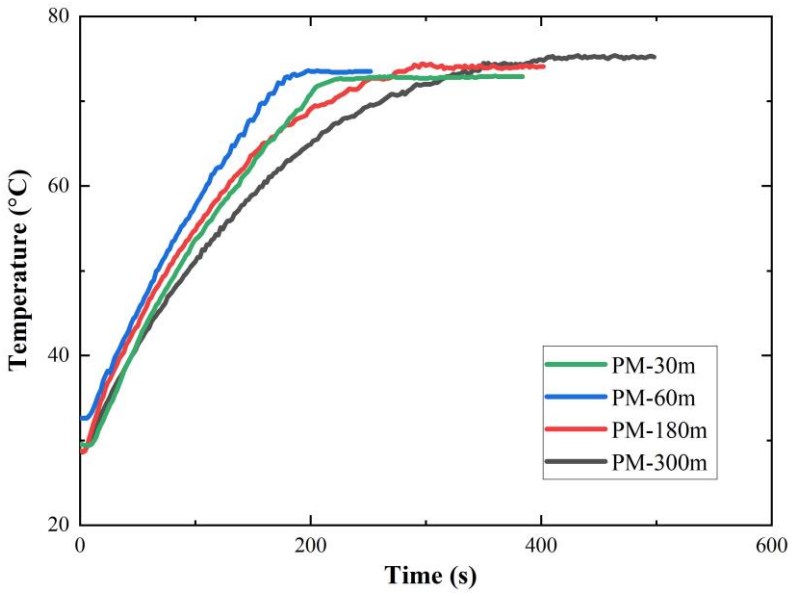

Figure 5.21. T-t plot of the hydrogenated LaFeSi samples by ball milling with different durations.

Table 5.10. Calculated SAR values for hydrogenated LaFeSi samples via ball-milling.

Samples	SAR (W/g)
PM-30m	58 ±1
PM-60m	60 ±3
PM-180m	119 ±3
PM-300m	111 ±6

6. DISCUSSION

$La(FeSi)_{13}$ compound is one of the promising magnetocaloric material with high saturation magnetization and tunable Curie temperature via light atom insertion [71]. In this study, $LaFe_{11.57}Si_{1.43}$ samples are synthesized via arc-melting method, following with annealing for 10 days within quartz capsules filled with Ar gas. Later, the samples are hydrogenated via Sievert-type apparatus and ball-milling. The structure of the samples hydrogenated via ball-milling are shown to be unstable and samples contain high α-Fe phase. Whereas samples hydrogenetaed by Sievert are almost single $NaZn_{13}$-type cubic phase with much higher purity (%94.4 $LaFe_{11.57}Si_{1.43}$) when compared to previous works [32],[34],[40]. The saturation magnetization of parent $LaFe_{11.57}Si_{1.43}$ at 10 K was found 158 emu/g, which is in good aggrement with previous reports [32]. Samples shows 1st-order magnetic phase transition where T_C point is successfully controlled by adjusting the hydrogenation insertion via vacuum-heating. The Curie Temperature of the samples are adjusted in the 195 K to 319 K range and auto-control heating performance of the material in a liquid media under AMF is succesfully demonstrated. After hydrogen insertion at 200˚C, lattice constant increased from 11.4483 Å to 11.6211 Å [59].

The effectiveness of inducing cell death through hyperthermia (41 to 43 °C) is generally lower compared to thermo-ablation (above 45 °C) [73]. Hyperthermia alone may result in tumor re-growth due to cancer cell recovery after apoptosis [73]. In a study by K.A. Court et al., magnetic fluid hyperthermia was applied to ovarian cancer cells using carboxymethyl dextran-coated iron oxide nanoparticles under an alternating magnetic field (AMF) of 24 and 36 kA/m (245 kHz). The temperature reached 43 °C in 30 minutes, leading to the upregulation of heat shock protein (HSP) genes implicated in tumor cell proliferation [74]. In the current work, the temperature rises to 50 °C in less than 7 minutes in the magnetic fluid using the synthesized $La(FeSi)_{13}H_{1.41}$ sample. Given the significant heating efficacy of magnetic nanoparticles, this performance is excellent for potentially preventing tumor re-growth. The rapid temperature increase in the magnetic fluid under the influence of $La(FeSi)_{13}H_{1.41}$ nanoparticles highlights the potential of this material for efficient hyperthermia applications in cancer treatment.

Although the $LaFe_{11.57}Si_{1.43}H_{1.41}$ material synthesized in this research study shows great potential for non-invasive cancer treatment applications in the future, there are areas that

require improvement, such as hydrogen insertion, particle size reduction and surface functionalization. The findings indicate that the heating and subsequent cooling processes impact the stability of the material, particularly the first-order phase transition. To address this, adjusting the hydrogen level during the hydrogenation process after determining the optimum hydrogen gas volume for a specific mass of the material may help maintain structural stability and preserve a rapid first-order phase transition, resulting in better auto-control performance. For achieving a finer particle size, parameters such as milling time, speed, interval duration, and period for the ball-milling method can be optimized. Size separation techniques may be employed to minimize the size distribution in future studies [76]. To ensure good dispersion of particles in water, surface coating with a hydrophobic and biocompatible material, such as silica can be investigated [77]. Furthermore, auto-controlled magnetic hyperthermia, which irreversibly kills cancer cells in a short time, can be utilized in a hybrid approach. Tumor microenvironments vary depending on tumor sites, growth stages, and different patients. Combining auto-controlled MHT with immunotherapy could lead to a more personalized and faster treatment effect. In future studies, these mentioned improvements, along with clinical tests and research on mass-production methods, can be explored.

7. REFERENCES

1. Mansouri, V., et al., *Recent advances in regenerative medicine strategies for cancer treatment.* Biomedicine & Pharmacotherapy, 2021. **141**: p. 111875.
2. Liu, X., et al., *Comprehensive understanding of magnetic hyperthermia for improving antitumor therapeutic efficacy.* Theranostics, 2020. **10**(8): p. 3793.
3. Sharma, S., et al., *Nanoparticles-based magnetic and photo induced hyperthermia for cancer treatment.* Nano Today, 2019. **29**: p. 100795.
4. Chao, Y., et al., *Iron nanoparticles for low-power local magnetic hyperthermia in combination with immune checkpoint blockade for systemic antitumor therapy.* Nano letters, 2019. **19**(7): p. 4287-4296.
5. Du, Y., et al., *Optimization and design of magnetic ferrite nanoparticles with uniform tumor distribution for highly sensitive MRI/MPI performance and improved magnetic hyperthermia therapy.* Nano letters, 2019. **19**(6): p. 3618-3626.
6. Kawahara, I., et al., *Magnetic hyperthermia using self-controlled heating elements consisting of Fe-Al milling alloy induces cancer cell apoptosis while preserving skeletal muscle.* Pathobiology, 2019. **86**(5-6): p. 254-262.
7. Gilchrist, R., et al., *Selective inductive heating of lymph nodes.* Annals of surgery, 1957. **146**(4): p. 596.
8. Latorre, M. and C. Rinaldi, *Applications of magnetic nanoparticles in medicine: magnetic fluid hyperthermia.* Puerto Rico health sciences journal, 2009. **28**(3).
9. Yamamoto, Y., et al., *Size dependence study on magnetic heating properties of superparamagnetic iron oxide nanoparticles suspension.* Journal of Applied Physics, 2014. **116**(12).
10. Pucci, C., et al., *Superparamagnetic iron oxide nanoparticles for magnetic hyperthermia: Recent advancements, molecular effects, and future directions in the omics era.* Biomaterials Science, 2022. **10**(9): p. 2103-2121.
11. Veloso, S.R., R.G. Andrade, and E.M. Castanheira, *Review on the advancements of magnetic gels: towards multifunctional magnetic liposome-hydrogel composites for biomedical applications.* Advances in Colloid and Interface Science, 2021. **288**: p. 102351.
12. Rosensweig, R.E., *Heating magnetic fluid with alternating magnetic field.* Journal of magnetism and magnetic materials, 2002. **252**: p. 370-374.
13. Hannon, G., et al., *The effects of localized heat on the hallmarks of cancer.* Advanced Therapeutics, 2021. **4**(7): p. 2000267.
14. Heisterkamp, J., R. van Hillegersberg, and J.N. IJzermans, *Critical temperature and heating time for coagulation damage: implications for interstitial laser coagulation (ILC) of tumors.* Lasers in surgery and medicine, 1999. **25**(3): p. 257-262.
15. Yu, P.C., *First and Second Order Phase Transitions*. 2012, University of California Irvine, School of Physical Sciences: Physics 115A.
16. Hejase, H., et al., *MnZnFe nanoparticles for self-controlled magnetic hyperthermia.* Journal of Magnetism and Magnetic Materials, 2012. **324**(22): p. 3620-3628.
17. Prasad, N., et al., *TC-tuned biocompatible suspension of La0. 73Sr0. 27MnO3 for magnetic hyperthermia.* Journal of Biomedical Materials Research Part B: Applied Biomaterials: An Official Journal of The Society for Biomaterials, The Japanese Society for Biomaterials, and The Australian Society for Biomaterials and the Korean Society for Biomaterials, 2008. **85**(2): p. 409-416.

18. Kuznetsov, A.A., et al., *Local radiofrequency-induced hyperthermia using CuNi nanoparticles with therapeutically suitable Curie temperature.* Journal of Magnetism and Magnetic Materials, 2007. **311**(1): p. 197-203.
19. Akin, Y., et al., *Ni1-x Crx alloy for self controlled magnetic hyperthermia.* Crystal Research and Technology: Journal of Experimental and Industrial Crystallography, 2009. **44**(4): p. 386-390.
20. Mohite, V., *Self controlled magnetic hyperthermia.* 2004.
21. Pereira, P.L., et al., *Radiofrequency ablation: the percutaneous approach.* Minimally Invasive Tumor Therapies, 2006: p. 39-52.
22. Soetaert, F., et al., *Computational evaluation of amplitude modulation for enhanced magnetic nanoparticle hyperthermia.* Biomedical Engineering/Biomedizinische Technik, 2015. **60**(5): p. 491-504.
23. Kandala, S.K., et al., *Temperature-controlled power modulation compensates for heterogeneous nanoparticle distributions: a computational optimization analysis for magnetic hyperthermia.* International Journal of Hyperthermia, 2018.
24. Sharma, A., et al., *Design of a temperature-feedback controlled automated magnetic hyperthermia therapy device.* Frontiers in thermal engineering, 2023. **3**: p. 1131262.
25. Raghavan, V., *Fe-La-Si (iron-lanthanum-silicon).* Journal of Phase Equilibria and Diffusion, 2001. **22**(2): p. 158.
26. Han, M.-K. and G.J. Miller, *An Application of the "Coloring Problem": Structure− Composition− Bonding Relationships in the Magnetocaloric Materials LaFe13-x Si x.* Inorganic chemistry, 2008. **47**(2): p. 515-528.
27. Tang, Z., et al., *Structural and magnetic properties of LaFe 13-x Si x nitrides.* 1993.
28. Liu, X., et al., *Phase formation and structure in rapidly quenched La (Fe0. 88Co0. 12) 13− xSix alloys.* Journal of alloys and compounds, 2005. **397**(1-2): p. 120-125.
29. Gębara, P., et al., *The evolution of microstructure in annealed LaFeSi-type alloys.* Optica Applicata, 2009. **39**(4): p. 761-764.
30. Chen, X., Y. Chen, and Y. Tang, *The studies of high-temperature and short-time annealing, phase transition process, and magnetic property for LaFe11. 7Si1. 3 compound.* Phase Transitions, 2012. **85**(1-2): p. 27-40.
31. Niitsu, K., et al., *Microstructure and magnetic properties of as-quenched cubic and tetragonal La (Fe1− xSix) 13 compounds.* Journal of alloys and compounds, 2013. **578**: p. 220-227.
32. Phejar, M., V. Paul-Boncour, and L. Bessais, *Magnetocaloric study of mechanically alloyed LaFeSi.* Minerals, Metals and Materials Society/AIME, 420 Commonwealth Dr., P. O. Box 430 Warrendale PA 15086 United States.[np]. Feb, 2011.
33. Thayer, A., et al., *Synthesis and magnetic properties of LaFe13-x-yMxSiyN3 nitrides.* Journal of Alloys and Compounds, 2022. **920**: p. 165927.
34. Paul-Boncour, V. and L. Bessais, *Tuning the magnetocaloric properties of the La (Fe, Si) 13 compounds by chemical substitution and light element insertion.* Magnetochemistry, 2021. **7**(1): p. 13.
35. Zong, S., et al., *The effect of segregation on the Curie temperature in large-sized La-Fe-Co-Si alloys.* Journal of Magnetism and Magnetic Materials, 2018. **461**: p. 111-115.

36. Shen, J., et al., *Reduction in hysteresis losses and large magnetic entropy change in the B-doped La (Fe, Si) 13 compounds.* Journal of Applied Physics, 2010. **107**(9).
37. Huang, M., et al., *Magnetic properties and structure of nitrogenated La (Co/sub 1-x/Fe/sub x/)/sub 13/compounds (x= 0-0.4).* IEEE transactions on magnetics, 1992. **28**(5): p. 2859-2861.
38. Terwey, A., et al., *Influence of hydrogenation on the vibrational density of states of magnetocaloric LaFe 11.4 Si 1.6 H 1.6.* Physical Review B, 2020. **101**(6): p. 064415.
39. Jia, L., et al., *Volume dependence of the magnetic coupling in LaFe13− xSix based compounds.* Applied Physics Letters, 2008. **92**(10).
40. Mandal, K., et al., *Effect of reactive milling in hydrogen on the magnetic and magnetocaloric properties of LaFe11. 57Si1. 43.* Journal of magnetism and magnetic materials, 2005. **290**: p. 673-675.
41. Bez, H.N., et al., *Magnetocaloric effect and H gradient in bulk La (Fe, Si) 13Hy magnetic refrigerants obtained by HDSH.* Journal of Magnetism and Magnetic Materials, 2015. **386**: p. 125-128.
42. Barsuk, D., *Metallurgical Design of New Nanoporous Structures*. 2017, Universidade federal de São Carlos.
43. EdmundBühler, *Compact Arc Melter MAM-1*. www.edmund-buehler.de/.
44. Retsch, *PLANETARY BALL MILL PM-400*. www.retsch.com.
45. Policicchio, A., et al., *Volumetric apparatus for hydrogen adsorption and diffusion measurements: Sources of systematic error and impact of their experimental resolutions.* Review of scientific instruments, 2013. **84**(10).
46. Gross, K., *The PCTPro-2000-The Ultimate Tool for Gas Sorption Analysis.* Material Matters, 2007. **2**(2): p. 26-28.
47. Ntsendwana, B., *Advanced low temperature metal hydride materials for low temperature proton exchange membrane fuel cell application*. 2010, University of the Western Cape.
48. Boateng, E. and A. Chen, *Recent advances in nanomaterial-based solid-state hydrogen storage.* Materials Today Advances, 2020. **6**: p. 100022.
49. Sulochanadevi, B., *Structure and Regulation of Yeast Glycogen Synthase*. 2010, thesis.
50. MalvernPanalytical, *Empyrean X-ray diffractometer*. www.directindustry.com/prod/malvern-panalytical/product-14669-1931584.html.
51. Inkson, B.J., *Scanning electron microscopy (SEM) and transmission electron microscopy (TEM) for materials characterization*, in *Materials characterization using nondestructive evaluation (NDE) methods*. 2016, Elsevier. p. 17-43.
52. *Tescan GAIA3 SEM and Oxford XMax 150 EDS*. hunitek.hacettepe.edu.tr/fib-sem.
53. *Vibrating-sample magnetometer*, Wikipedia, access date: 2023.
54. Shah, S.A.H., *Vibrating Sample Magnetometery: Analysis and Construction*, in *Department of Physics, Syed Babar Ali School of Science and Engineering*. 2014, Lahore University of Management Sciences: https://physlab.org/story/vibrating-sample-magnetometry-analysis-and-construction/.
55. Grössinger, R., *Characterisation of hard magnetic materials.* Journal of Electrical Engineering, 2008. **59**(7): p. 15-20.

56. Ovejero, J.G., *Aggregation effects in iron oxide nanoparticles for Hyperthermia*, in *Science Faculty*. 2013, Universidad Autónoma de Madrid.
57. Goya, G., et al. *Magnetic structure and power absorption in magnetite nanoparticles from a MRI contrast agent*. in *Proc. IEEE Magn. Conf.(INTERMAG)*. 2006.
58. Yang, L., et al., *Peritectic solidification path of the La (Fe, Si)13 phase in dual-phase directionally solidified La-Fe-Si magnetocaloric alloys.* Metallurgical and Materials Transactions A, 2017. **48**: p. 4229-4236.
59. Bin, F., et al., *Hydrogen absorption of LaFe11. 5Si1. 5 compound under low hydrogen gas pressure.* Chinese Physics B, 2009. **18**(10): p. 4506.
60. Jia, L., et al., *Influence of interstitial and substitutional atoms on the crystal structure of La (FeSi) 13.* Journal of Alloys and Compounds, 2011. **509**(19): p. 5804-5809.
61. Hai, X., *Magnetocaloric materials for magnetic refrigeration at room temperature*. 2016, Université Grenoble Alpes.
62. Gong, P., et al., *Hydrogen embrittlement through the formation of low-energy dislocation nanostructures in nanoprecipitation-strengthened steels.* Science Advances, 2020. **6**(46): p. eabb6152.
63. Ghasemi, S., et al., *Crack evolution in damage stress thresholds in different minerals of granite rock.* Rock Mechanics and Rock Engineering, 2020. **53**: p. 1163-1178.
64. Chen, Y., et al., *Irreversible hydrogen embrittlement study of B1500HS high strength boron steel.* Materials & Design, 2021. **199**: p. 109404.
65. Maensiri, S. and S. Roberts, *Thermal shock of ground and polished alumina and Al2O3/SiC nanocomposites.* Journal of the European Ceramic Society, 2002. **22**(16): p. 2945-2956.
66. Fujita, A., S. Fujieda, and K. Fukamichi, *Influence of hydrogenation on the electronic structure and the itinerant-electron metamagnetic transition in strong magnetocaloric compound La (Fe0. 88Si0. 12) 13.* Journal of magnetism and magnetic materials, 2009. **321**(21): p. 3553-3558.
67. Baron, V., et al., *The influence of iron substitution in the magnetic properties of hausmannite, Mn (super 2+)(Fe, Mn)(super 3+) 2 O 4.* American Mineralogist, 1998. **83**(7-8): p. 786-793.
68. Parida, S., et al., *Influence of ball milling parameters on the crystallite size of Ba (Ti1-xZrx) O3.* Ferroelectrics, 2012. **429**(1): p. 22-30.
69. Chuan Lim, E.W. and R. Feng, Agglomeration of magnetic nanoparticles. The Journal of chemical physics, 2012. 136(12).
70. Tang, W., et al., *Particle size effects on La0. 7Ca0. 3MnO3: size-induced changes of magnetic phase transition order and magnetocaloric study.* Journal of magnetism and magnetic materials, 2010. **322**(16): p. 2360-2368.
71. Fujieda, S., A. Fujita, and K. Fukamichi, *Large magnetocaloric effect in La (Fe x Si 1− x) 13 itinerant-electron metamagnetic compounds.* Applied Physics Letters, 2002. **81**(7): p. 1276-1278.
72. Mandal, K., et al., *Magnetocaloric effect in reactively-milled LaFe11. 57Si1. 43Hy intermetallic compounds.* Journal of Applied Physics, 2007. **102**(5).
73. Vilas-Boas, V., F. Carvalho, and B. Espiña, *Magnetic hyperthermia for cancer treatment: Main parameters affecting the outcome of in vitro and in vivo studies.* Molecules, 2020. **25**(12): p. 2874.

74. Court, K.A., et al., *HSP70 inhibition synergistically enhances the effects of magnetic fluid hyperthermia in ovarian cancer.* Molecular cancer therapeutics, 2017. **16**(5): p. 966-976.
75. Ciocca, D.R. and S.K. Calderwood, *Heat shock proteins in cancer: diagnostic, prognostic, predictive, and treatment implications.* Cell stress & chaperones, 2005. **10**(2): p. 86.
76. Mori, Y., *Size-selective separation techniques for nanoparticles in liquid.* KONA powder and particle journal, 2015. **32**: p. 102-114.
77. Bharti, C., et al., *Mesoporous silica nanoparticles in target drug delivery system: A review.* International journal of pharmaceutical investigation, 2015. **5**(3): p. 124.

APPENDIX

A 1 – Conference Oral Presentation

"Self-Regulating Magnetic Hyperthermia Applications of LaFeSi Nanoparticles" oral presentation, 26-28 May 2023, Brussels-Belgium, 2nd World Conference on Materials Science and Nanotechnology